

# **Hafnium Dioxide Nanoparticle Thin Film Morphology and Reactivity with Dimethyl Methylphosphonate**

Allyn K. Milojevich

A thesis submitted to the faculty of the  
Virginia Polytechnic Institute and State University  
in partial fulfillment of the requirements for the degree of

MASTER OF SCIENCE

in

Chemistry

John R. Morris, Chair  
Karen Brewer  
John Dillard

November 28, 2006  
Blacksburg, Virginia

Keywords: hafnium dioxide, organophosphonate,  
dimethyl methylphosphonate

# **Hafnium Dioxide Nanoparticle Thin Film Morphology and Reactivity with Dimethyl Methylphosphonate**

Allyn K. Milojevich

## **ABSTRACT**

Organophosphonates have been used as simulants of highly toxic compounds such as chemical warfare agents in the study of the decomposition reactions that occur on the surface of hafnium dioxide. Metal oxide and metal-oxide nanoparticles have been shown to decompose organophosphonate molecules. In this study, high surface area hafnium oxide nanoparticles are synthesized via laser ablation. This creates nanoparticles that are free of contaminants and have a narrow size distribution. The particles are characterized by atomic force microscopy and scanning electron microscopy to determine particle size and thin film morphology. Once characterized, they are exposed to dimethyl methylphosphonate and the surface reaction is analyzed by reflection-absorption infrared spectroscopy.

## Acknowledgements

I would first and foremost like to thank Dr. John Morris for his support, guidance, and most importantly, patience during my graduate career at Virginia Tech. Without this guidance I would not be where I am today. I would also like to thank my committee members, Dr. Karen Brewer and Dr. John Dillard, for their guidance and advice throughout the past two years. I would also like to acknowledge Dr. Tissue for sharing his equipment and Wesley Gordon for his guidance and patience in teaching me how to run experiments and dealing with my excessive need for troubleshooting experimental setups and computer glitches. Frank Cromer and Steve McCartney have been very helpful in obtaining XPS data and SEM images.

The past and present members of the Morris group that made the daily grind of graduate school bearable, and I have been lucky enough to count many of them as wonderful friends: Melinda McPherson, Scott Day, Wes Gordon, Larry Fieglund, Josh Uzarski, Jessica Lu, Megan Bennett, and Erin Durke. During my time at Virginia Tech, I have made some of my best friends, and without them to encourage me when things got tough and cheer me up when things looked gloomy, I know I wouldn't be writing at all. I especially need to thank Dr. Matthew Mongelli and David Zigler, who without their wit, helpful discussions, and cheerful misdemeanor I couldn't have survived.

Lastly, I need to thank my mother, Deborah Risko, who has supported my academic endeavors throughout college and graduate school, without which I really wouldn't have ever gotten to this stage in my life. This is also dedicated to the memory of my father, Dan Milojevich, whose memory has served as a constant reminder of how I want to live my life. RIP 02-17-99

# Table of Contents

Chapter I Introduction and Motivation.....	1
1.1 Thesis Statement.....	1
1.2 Chemical Warfare Agents.....	1
1.3 Chemical Warfare Agent Simulants.....	5
1.4 Nanoparticles.....	6
1.5 Metal Oxide Nanoparticles.....	7
1.5.1 MgO.....	8
1.5.2 Al <sub>2</sub> O <sub>3</sub> .....	11
1.5.3 TiO <sub>2</sub> .....	11
1.5.4 Fe <sub>2</sub> O <sub>3</sub> .....	12
1.6 Inert Gas Phase Condensation of Nanoparticles.....	14
1.7 Hafnium Dioxide.....	15
1.8 Conclusion.....	16
Chapter II Experimental Approach.....	18
2.1 Inert-Gas Phase Condensation.....	18
2.2 Atomic Force Microscopy.....	19
2.3 Scanning Electron Microscopy.....	21
2.4 Nanoparticle Synthesis and Ultra-High Vacuum Analysis.....	22
2.5 Dimethyl Methylphosphonate (DMMP) Exposure Studies.....	23
2.6 X-ray Photoelectron Spectroscopy (XPS).....	25
2.7 Reflection-Absorption Infrared Spectroscopy (RAIRS).....	26
Chapter III Analysis of Hafnium Dioxide Nanoparticles:	
Particle Size and Thin Film Morphology.....	28
3.1 Introduction.....	28
3.2 Experimental Setup.....	28
3.3 Particle Size Analysis.....	29
3.4 Microscopic Film Morphology.....	32
3.5 Conclusion.....	36
Chapter IV Reactivity of Hafnium Dioxide Nanoparticles with	
Dimethyl Methylphosphonate.....	37
4.1 Introduction.....	37
4.2 Exposure studies.....	38
4.2.1 DMMP on a Gold Substrate.....	38
4.2.2 DMMP on a Cold Gold Substrate.....	38
4.2.3 X-ray Photoelectron Spectroscopy Characterization.....	39
4.2.4 Infrared Characterization of Hafnium Dioxide Nanoparticles.....	40
4.2.5 DMMP Uptake on 2.3 nm Hafnium Dioxide Nanoparticles.....	42
4.2.6 Methanol Exposure to 1.2 nm Hafnium Dioxide Nanoparticles. . . . .	48
4.2.7 TMP Exposure to 1.2 nm Hafnium Dioxide Nanoparticles . . . . .	50
4.2.8 Deuterated DMMP on 2.3 nm Hafnium Dioxide Nanoparticles... . . . .	52
4.2.9 Surface Bound Products.....	53

## Table of Contents continued

4.2.10 DMMP on 1.2 nm Hafnium Dioxide Nanoparticles.....	55
4.2.11 Hafnium Dioxide Nanoparticles made in an Oxygen Backfill .....	57
4.2.12 Hafnium Dioxide Nanoparticles Annealed to 500K and then Exposed to DMMP.....	59
4.3 Conclusions.....	62
4.4 Future Work.....	65
References.....	67

## List of Figures

Figure 1.1	Common chemical warfare agents sarin, VX, soman, and mustard gas ....2
Figure 1.2	Oxidation of mustard gas to sulfoxide using water and hydrogen peroxide.....3
Figure 1.3	Nucleophilic replacement of fluorine on sarin with hydroxide using peroxides.....4
Figure 1.4	Hydrolysis of VX at the phosphorus-sulfur bond using peroxide.....5
Figure 1.5	Common chemical warfare agent simulants, trimethyl methylphosphonate, dimethyl methylphosphonate, and 2-chloroethyl ethylsulfide that mimic different agents and different chemical functionalities of agents.....5
Figure 1.6	Doubling the diameter of a cube decreases the surface area : volume ratio significantly.....7
Figure 1.7	Various surface species resulting from the adsorption of small molecules on a metal oxide. Metal oxides are capable of binding molecules as both mono- and bi-dentate species.....8
Figure 1.8	Electrophilic attack of a metal oxide surface on using residual surface hydroxyl functionalities.....11
Figure 1.9	Nucleophilic attack of the surface on DMMP and the Mars and Van Krevelen mechanism for regenerating a fully oxidized surface.....13
Figure 2.1	Diagram of the inert gas phase condensation setup using a 40W CO <sub>2</sub> laser beam to ablate a bulk HfO <sub>2</sub> pellet and collect the nanoparticles on a suspended substrate.....19
Figure 2.2	Schematic of an AFM measurement used to analyze nanoparticles size...21

## List of Figures continued

Figure 2.3	The basic schematic of an SEM instrument.....	22
Figure 2.4	Setup of nanoparticle synthesis with adjacent ultra-high vacuum analysis instrumentation, including RAIRS, XPS, and a residual gas analyzer.....	23
Figure 2.5	A stream of argon bubbles through a reservoir of DMMP heated to 90°C and carried through a series of heated nalgene tubes to a heated leak valve.....	24
Figure 2.6	Energy level diagrams for X-ray Photoelectron Spectroscopy.....	25
Figure 2.7	Visual representation of electronic field vectors.....	27
Figure 3.1	AFM height image of a 1 µm by 1 µm area of silicon wafer with dispersed hafnium dioxide nanoparticles.....	29
Figure 3.2	Cross section and height analysis for a set of nanoparticles.....	30
Figure 3.3	Distribution of sizes of particles created in 1 and 10 Torr of nitrogen.....	31
Figure 3.4	Distribution of hafnium dioxide nanoparticle sizes when synthesized in oxygen.....	32
Figure 3.5	Nanoparticle thin film morphology created in one Torr of nitrogen at 500x, 5,000x, 10,000x, and 20,000x magnifications.....	33
Figure 3.6	SEM images of nanoparticles formed in 2, 3, 4, and 5 Torr of nitrogen at 5,000x magnification.....	34
Figure 3.7	Hafnium dioxide nanoparticles formed in 1 Torr of nitrogen on a methyl terminated, hydrophobic self-assembled monolayer surface and a hydroxyl terminated, hydrophilic self-assembled monolayer surface.....	35

## List of Figures continued

Figure 3.8	Edge defects of thin films formed in 1 Torr of nitrogen.....	35
Figure 4.1	Chemical structures of sarin, soman, and DMMP, the simulant used in this study.....	37
Figure 4.2	XPS spectrum of hafnium dioxide nanoparticles before exposure to DMMP.....	39
Figure 4.3	Hafnium dioxide nanoparticles before exposure to DMMP.....	41
Figure 4.4	Carbon and phosphorus areas of the XPS spectrum before and after DMMP exposure.....	43
Figure 4.5	Gas phase DMMP spectrum compared to DMMP adsorbed on 2.3 nm hafnium dioxide nanoparticles.....	44
Figure 4.6	C-H stretching region of the gas phase DMMP spectrum and the spectrum of DMMP adsorbed on to hafnium dioxide nanoparticles.....	45
Figure 4.7	Lower frequency region of the gas phase DMMP and DMMP adsorbed on HfO <sub>2</sub> spectrum.....	47
Figure 4.8	High frequency region of methanol adsorbed on 1.2 nm hafnium dioxide nanoparticles.....	49
Figure 4.9	Low frequency region of methanol adsorbed on 1.2 nm hafnium dioxide nanoparticles.....	49
Figure 4.10	Structures of TMP and DMMP.....	50
Figure 4.11	High frequency spectrum of TMP on 1.2 nm hafnium dioxide nanoparticles.....	51

## List of Figures continued

Figure 4.12	Low frequency spectrum of TMP on 1.2 nm hafnium dioxide nanoparticles.....	52
Figure 4.13	Deuterated DMMP.....	52
Figure 4.14	High frequency C-H and C-D stretching region of deuterated DMMP on 2.3 nm hafnium dioxide nanoparticles.....	53
Figure 4.15	Two different fates of DMMP on a hafnium dioxide surface.....	54
Figure 4.16	Time dependent spectra as a function of exposure varying from 30 Langmuir to 130 Langmuir.....	55
Figure 4.17	Comparison of gas phase DMMP to DMMP adsorption on 1.2 nm hafnium dioxide nanoparticles at room temperature.....	56
Figure 4.18	Comparison of DMMP reactivity after 130 Langmuir of exposure on larger and smaller hafnium dioxide nanoparticles.....	57
Figure 4.19	High frequency region of DMMP adsorbed on oxygen synthesized 3.2 nm hafnium dioxide nanoparticles.....	58
Figure 4.20	Comparison of DMMP exposed to larger, oxygen synthesized nanoparticles and smaller, nitrogen synthesized nanoparticles.....	59
Figure 4.21	Comparison of DMMP adsorption on annealed and cooled nanoparticles and unannealed nanoparticles.....	60
Figure 4.22	C-H stretching region of DMMP adsorption on 2.3 nm HfO <sub>2</sub> nanoparticles at difference exposures.....	61
Figure 4.23	DMMP adsorbs and reacts on HfO <sub>2</sub> nanoparticles at room temperature...	64
Figure 4.24	Possible mechanism of DMMP reacting on HfO <sub>2</sub> .....	65

## List of Tables

Table 1.1	Nerve agent physical properties.....	2
Table 1.2	Nerve agent toxicology.....	2
Table 1.3	Physical properties of chemical warfare agent simulants.....	6
Table 1.4	Toxicology of chemical warfare agent simulants.....	6
Table 4.1	Expected atomic percentages versus actual atomic percentages.....	40
Table 4.2	Atomic percentages via XPS analysis after DMMP exposure.....	43

## List of Abbreviations

DMMP	Dimethyl Mmthylphosponate
CWA	Chemical warfare agent
UHV	Ultra-high vacuum
AFM	Atomic force microscopy
SEM	Scanning Electron Microscopy
XPS	X-ray Photoelectron Spectroscopy
RAIRS	Reflection-Absorption Infrared Spectroscopy
TMP	Trimethyl methylphosponate

# Chapter One

## Introduction and Motivation

### 1.1 Thesis Statement

The purpose of this study is to determine the mechanism of interaction between dimethyl methylphosphonate (DMMP), a common chemical warfare agent stimulant, and hafnium dioxide nanoparticles and to understand how surface functionalities affect uptake and reactivity.

### 1.2 Chemical Warfare Agents

Large quantities of chemical warfare agents (CWAs) are stockpiled in the United States.<sup>1</sup> The U.S. has three major stockpiles of agents: mustard gas (HD), VX, and sarin (GB). Mustard gas is a blister agent<sup>2</sup> that attacks the mucus membranes and can be lethal at high doses.<sup>3</sup> VX, sarin, and soman (GD) are nerve agents that stop respiratory and nervous functions and can kill a person within minutes. Although chemical warfare nerve agents are often referred to as nerve gases, they exist at room temperature as polar organic liquids with a low vapor pressure. Nerve agents are organophosphorus compounds that inhibit acetylcholine esterase from removing excess acetylcholine from nerve synapses, leading to respiratory and nervous system failure.<sup>4</sup>

The following tables show the chemical properties and toxicological properties of four common chemical warfare agents: VX, sarin, soman, and mustard gas, whose structures are shown in Figure 1.1. The  $LC_{50}$  refers to the amount of agent that is lethal for approximately 50% of the population, while the  $IC_{50}$  is the quantity that will incapacitate half of the population.<sup>4</sup> Toxicology values for inhalation are given in values

of  $\text{mg}\cdot\text{min}/\text{m}^3$ , while quantities for an ingestion route of exposure are presented with units of  $\text{mg}/\text{kg}$ .<sup>4</sup>

Name	Molecular Weight (g/mol) <sup>4</sup>	Melting Temperature (°C) <sup>4</sup>	Boiling Temperature (°C) <sup>4</sup>	Vapor Pressure (torr) at RT <sup>4</sup>	Decomposition Temperature (°C) <sup>4</sup>
<b>VX</b>	267.38	-51	298	0.0007	295
<b>Sarin</b>	140.09	-50	158	2.9	150
<b>Soman</b>	182.18	-42	198	0.40	130
<b>Mustard</b>	159.08	14.45	217	0.072	149

**Table 1.1 Nerve agent physical properties.**

Name	State at Room Temperature <sup>4</sup>	Rate of Action <sup>4</sup>	Route <sup>4</sup>	LC <sub>50</sub> <sup>4</sup> mg*min/m <sup>3</sup>	IC <sub>50</sub> <sup>4</sup> mg*min/m <sup>3</sup>
<b>VX</b>	colorless liquid	rapid	inhalation	100	50
			ingestion	1.0 mg/kg	
<b>Sarin</b>	colorless liquid	very rapid	inhalation	70	35
			skin absorption	12,000	8,000
			ingestion	0.01 mg/kg	
<b>Soman</b>	colorless liquid	very rapid	inhalation	100	35
			ingestions	0.01 mg/kg	
<b>Mustard</b>	colorless liquid	very rapid	inhalation	1500	10,000
			skin absorption	200	2,000

**Table 1.2 Nerve agent toxicology.**

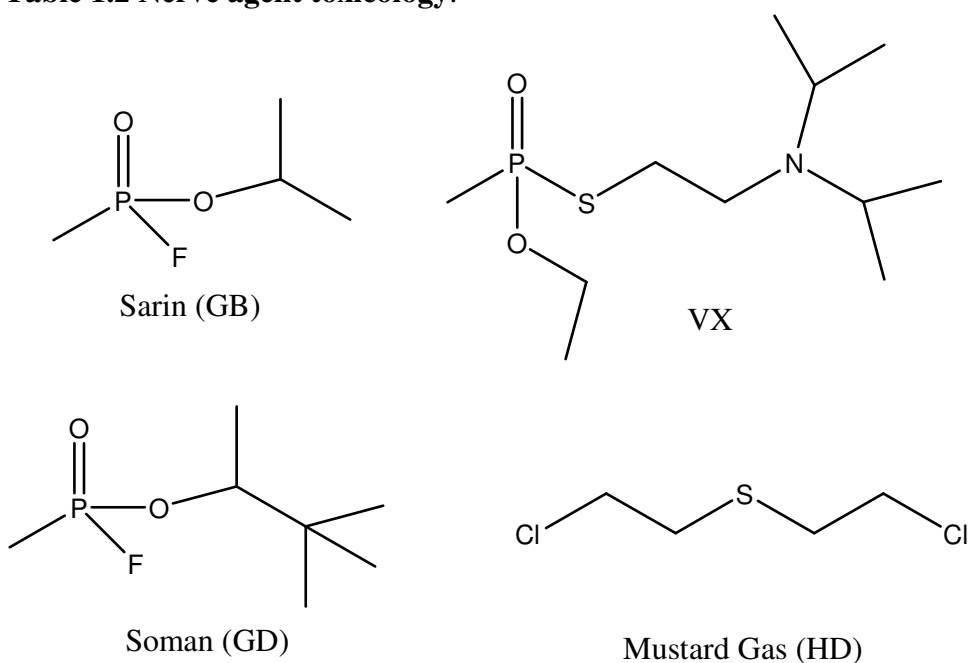


**Figure 1.1 Common chemical warfare agents sarin, VX, soman, and mustard gas.**

Disposal of chemical warfare agents is a highly active area of research.<sup>5</sup> Chemical warfare agents can either be incinerated or neutralized by chemical reactions. Neutralization involves the conversion of the agents into non-toxic or less toxic products<sup>6</sup> and is performed to decrease the chemical's toxicity before further disposal. One of the earliest needs for decontamination occurred in 1915 during World War I when Germany released mustard gas on Allied troops in Ypres.<sup>7</sup> Hydrolysis of mustard gas is relatively slow, proceeding by an S<sub>N</sub>1 reaction.<sup>8</sup> While hydrolysis occurs slowly, the oxidation of HD to sulfoxide occurs very rapidly,<sup>9</sup> and the product is then water soluble and more amenable to hydrolysis. To begin the chemical warfare agent hydrolysis, peroxide activators, such as bicarbonate, HCO<sub>3</sub><sup>-</sup>, form peroxy carbonate, HCO<sub>4</sub><sup>-</sup>, which selectively oxidizes mustard gas to its corresponding sulfoxide.<sup>10,11</sup> The reaction is shown in Figure 1.2. Peroxides are desirable reactants for decontamination due to their non-toxic nature<sup>12</sup> and are often used in “green” industrial processes.<sup>13</sup> This simple reaction involving hydrogen peroxide and bicarbonate is able to decompose mustard gas as well as the nerve agents sarin and VX.<sup>8</sup>

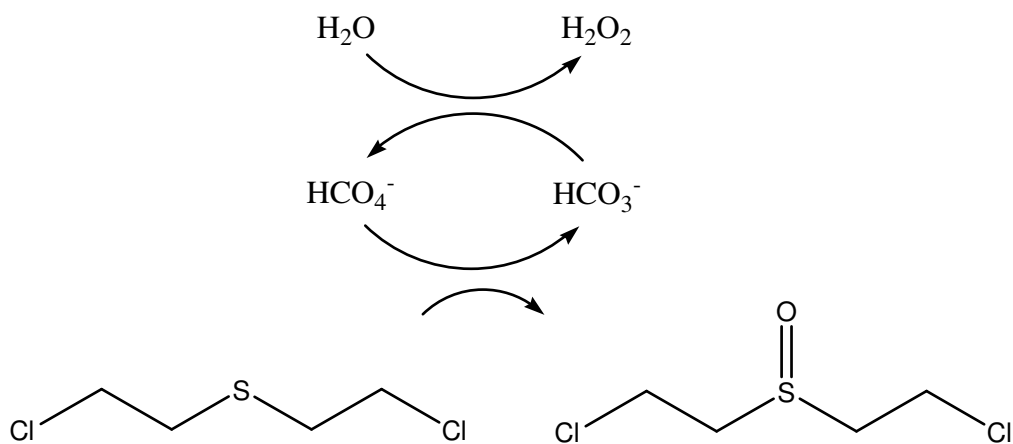


**Figure 1.2 Oxidation of mustard gas to sulfoxide using water and hydrogen peroxide.**

Peroxides quickly decompose sarin and soman via generation of the nucleophile peroxy anion, (OOH<sup>-</sup>).<sup>14,15</sup> The reaction, shown in Figure 1.3, consumes two moles of hydrogen peroxide and generates one mole of oxygen gas for each mole of reagent. In a solution containing only peroxide, the reaction has a half life of sixty-seven hours; however, addition of a small amount of sodium bicarbonate can increase the rate of reaction to a half life of less than one minute.<sup>10</sup>

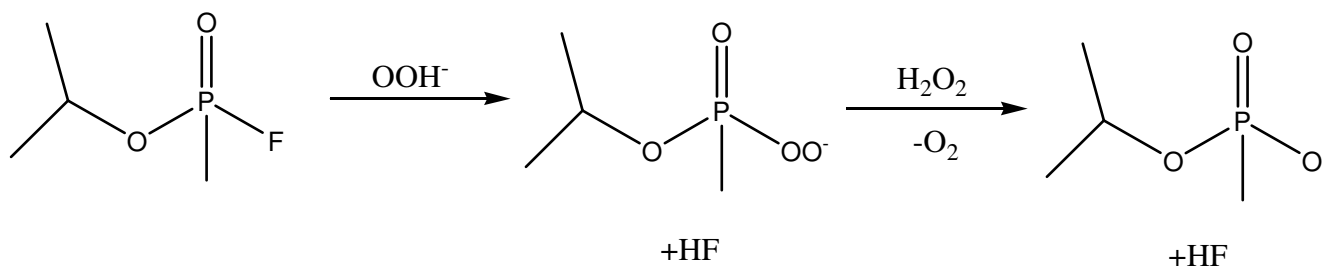


**Figure 1.3 Nucleophilic replacement of fluorine on sarin with hydroxide using peroxides.**

VX is much more persistent than other nerve agents due to its low vapor pressure<sup>17</sup> and is frequently decontaminated with profuse amounts of aqueous bleach, proceeding via hydrolysis at the P-S bond and simultaneous oxidation at the tertiary amino group.<sup>1</sup> Often, up to twenty moles of bleach are necessary for each mole of VX consumed.<sup>18</sup> Rather than using an excess of bleach, hydrolysis of VX using HO<sub>2</sub><sup>-</sup> as a strong nucleophile will selectively cleave the P-S bond, leaving water soluble residues shown in Figure 1.4 so the reaction does not produce additional solvent waste.<sup>15,19</sup>

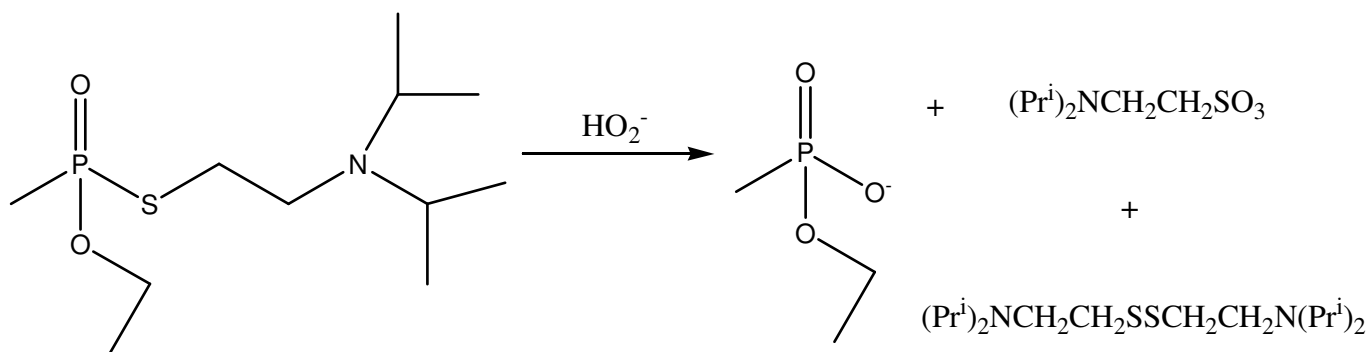


**Figure 1.4 Hydrolysis of VX at the phosphorus-sulfur bond using peroxide.**

### 1.3 Chemical Warfare Agent Simulants

To gain a complete understanding of the chemistry of chemical warfare agents, it is often desirable to use a series of analogs, shown in Figure 1.5, that mimic a certain chemical property of an agent, affording a systematic understanding of reactivity.

Chemical warfare agent simulants are less toxic than the real agents, so studying their interaction with nanoparticles may provide a detailed understanding of the reaction products and kinetic rate expressions that occur when chemical warfare agents interact with the same nanoparticle's surface.<sup>1</sup>

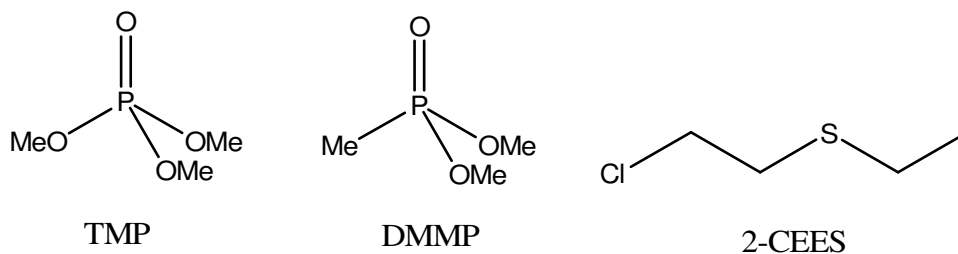


**Figure 1.5 Common chemical warfare agent simulants, trimethyl methylphosphonate, dimethyl methylphosphonate, and 2-chloroethyl ethylsulfide that mimic different agents and different chemical functionalities of agents.**

Name	Molecular Weight (g/mol)	Melting Temperature °C	Boiling Temperature °C	Vapor Pressure at RT (torr)
<b>TMP</b>	140.08	-46	197.2	1.22
<b>DMMP</b>	124.08	N/A	181	0.85
<b>2-CEES</b>	124.63	N/A	156	44

**Table 1.3 Physical properties of chemical warfare agent simulants.**

Name	State at Room Temperature	Route	LCt50 (mg/kg)
<b>DMMP</b>	colorless liquid	ingestion	5000
		skin adsorption	2000
<b>TMP</b>	colorless liquid	ingestion	1200
		skin adsorption	3352
<b>2-CEES</b>	colorless liquid	ingestion	252

**Table 1.4 Toxicology of chemical warfare agent simulants.**

#### 1.4 Nanoparticles

Nanoparticles are of particular interest in chemical warfare agent decomposition because they often exhibit enhanced reactivity compared to bulk material when the electrons are confined in nano-sized particles,<sup>20</sup> especially semi-conductor nanoparticles, to spaces less than their deBroglie wavelength, typically between one and thirty nanometers.<sup>21</sup> The size of nanoparticles is very difficult to characterize because most spectroscopic techniques only reveal an average of the properties of the individual nanoparticles, with larger particles, perhaps larger than the nanoscale range, having greater influence.<sup>22</sup> One of the features that make nanoparticles so interesting is the high proportion of surface atoms they contain. It is expected that nanoparticles would likely adapt a spherical morphology in order to minimize their surface energy, hence lowering their overall energy. Assuming spherical particles with the average radius  $r_{av}$  and bulk density  $\rho$ , the surface area per unit mass,  $\sigma$ , may be estimated by:

$$\sigma = \frac{3}{\rho r_{av}}$$

This quantity increases as the overall size of the nanoparticle decreases. So as the size of the nanoparticle increases, the ratio of surface area to volume decreases.

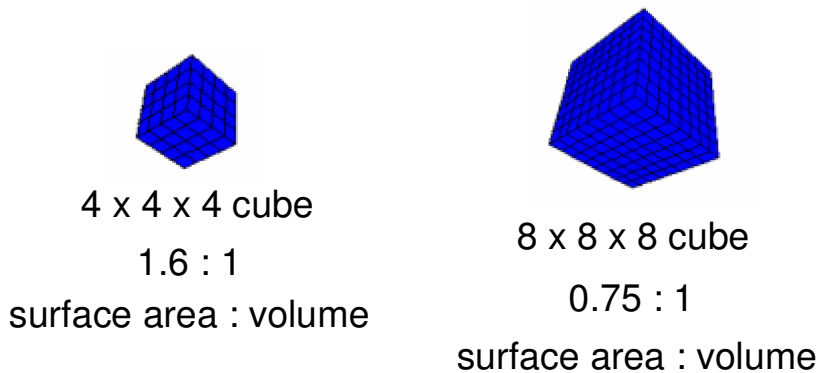


**Figure 1.6 Doubling the diameter of a cube decreases the surface area : volume ratio significantly.**

The regime of “nanoparticles” falls between the classical fields of chemistry, with sizes between 0.5 nm and 2 nm, and solid state physics, 10 nm up to bulk. In the intermediate region, between 2 nm and 10 nm, neither the rules of quantum mechanics nor classical physics apply.<sup>23</sup>

### 1.5 Metal Oxide Nanoparticles

One feature of nanoparticles is their increased reactivity compared to analogous bulk material.<sup>24</sup> This property makes metal oxide nanoparticles excellent destructive adsorbents. This term is intended to convey the ability to efficiently adsorb and simultaneously destroy the incoming adsorbate. Nanometer-scale materials also feature high surface areas, enhancing their capabilities as sorbents. Features such as high surface areas have led researchers to study nanoparticulate metal oxides, such as MgO, Al<sub>2</sub>O<sub>3</sub>, TiO<sub>2</sub>, and Fe<sub>2</sub>O<sub>3</sub>, as destructive sorbents for chemical warfare agents.

### 1.5.1 MgO

Magnesium oxide is highly ionic and has a high melting point. The  $\text{Mg}^{2+}$  ions in the lattice act as strong Lewis acids, while the  $\text{O}^{2-}$  ions act as Lewis bases with excess electron density. The Lewis acid and base sites can strongly interact with impinging polar molecules. In studies performed at Kansas State University, Klabunde et al. have shown that MgO nanocrystals have a high proportion of edge sites (a type of defect) as well as residual surface  $-\text{OH}$  groups, even after annealing.<sup>25</sup> It was also shown that small acidic molecules, such as  $\text{CO}_2$ <sup>24</sup> and  $\text{NO}_2$ <sup>26</sup>, will chemisorb to the surface to form unidentate and bidentate surface species, illustrated in Figure 1.7.

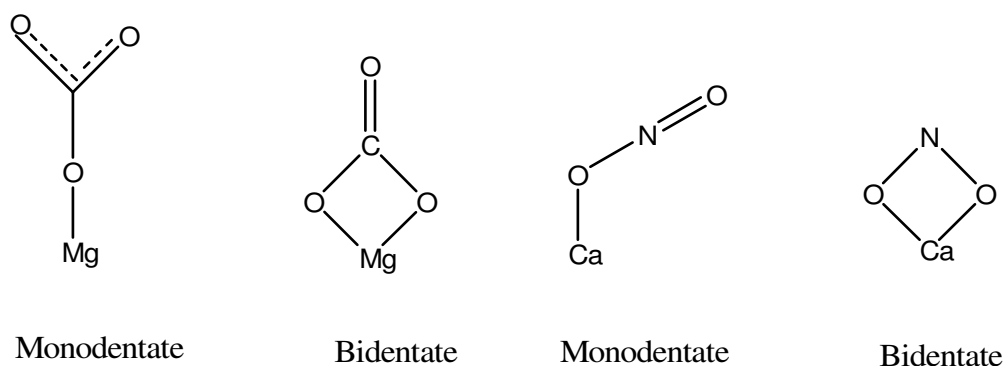


**Figure 1.7 Various surface species resulting from the adsorption of small molecules on a metal oxide. Metal oxides are capable of binding molecules as both mono- and bi-dentate species.**

Work at the Aberdeen Proving Ground using  $^{31}\text{P}$  and  $^{13}\text{C}$  NMR has shown that nanosized MgO can decompose VX, sarin, soman, and mustard gas at room temperature.<sup>27</sup> For the three organophosphorus compounds, selective hydrolysis occurs at the surface. For reactions with low percentages of CWA compared to MgO, a fast initial reaction was observed followed by a slower, diffusion-limited reaction with first-order kinetics. The fast reactions are attributed to the agents quickly reaching reactive sites upon exposure to the surface. The remaining reaction is attributed to CWA

molecules reaching reactive sites by diffusion across the surface.<sup>27</sup> The authors proposed that metal oxide nanoparticles could serve as a form of “hasty” decontamination on the battlefield.<sup>27</sup> The work was supported by a theoretical study of sarin on MgO.<sup>28</sup> The “atoms in molecules” (AIM) theory was used to determine which atoms are bonded in the system. It was determined that sarin only weakly binds to a perfect, crystalline MgO surface due to the formation of one C—H---O hydrogen bond and weak interactions between the oxygen ions of the MgO surface and the F of the sarin molecule. Edges and corners of the MgO lattice show increased surface reactivity.<sup>28</sup> When magnesium at a defect site is involved in the interaction, it forms a strong bond with the oxygen atom of sarin, resulting in chemisorbed sarin. The authors proposed a mechanism in which the electronegative fluorine strongly interacts with residual surface hydroxyl groups, resulting in cleavage of the P-F bond and subsequent release of HF. The oxygen from the hydroxyl group then contributes to a bridging sarin residue.<sup>28</sup> This result has also occurs when sarin interacts with Al<sub>2</sub>O<sub>3</sub>.<sup>28</sup> Theoretical studies of DMMP on magnesium oxide have shown that a bridging O-P-O species with a surface bound methoxy is stable,<sup>29</sup> supporting the hypothesis that sarin can form a bridging surface species.

Klabunde has studied a series of organophosphorus compounds adsorbing to MgO and has determined that compounds with a P=O moiety adsorb the most strongly.<sup>30</sup> Coordinatively unsaturated edge and corner sites have the strongest Lewis acid or Lewis base characteristics due to the presence of edge and corner vacancies.<sup>31</sup> Gas phase DMMP was exposed to nanocrystalline MgO and the surface chemical functionalities were monitored using surface IR. Upon observation by IR, the  $\nu(\text{P}=\text{O})$  peak shifted from 1242 to 1184  $\text{cm}^{-1}$ , indicating that the bond has significantly altered upon adsorption and

takes on more single bond character.<sup>32</sup> The  $\nu(\text{C-O-P})$  peak at  $1035\text{ cm}^{-1}$  is not significantly shifted, leading to the conclusion that the C-O bond is not greatly involved with initial adsorption.<sup>32</sup> The authors also found that DMMP adsorbed on MgO would react to form a bridging O-P-O species and release gas-phase methanol upon heating to  $500\text{ }^{\circ}\text{C}$ . The  $\text{Mg}^{2+}$  Lewis acid site is hypothesized to be very important for initial binding.

Infrared studies have shown that no shifts in the C-H stretches were observed upon adsorption of DMMP on MgO from gas-phase DMMP.<sup>33</sup> Upon heating the sample to  $50\text{ }^{\circ}\text{C}$ , the C-H stretching bands associated with the methoxy modes shift to lower wavenumber. Further, heating to  $100\text{ }^{\circ}\text{C}$  resulted in the loss of half of the methoxy C-H stretch intensity, leaving the peaks with intensity similar to the methyl C-H stretching modes.<sup>33</sup> The methoxy stretching modes continue to decrease in intensity upon heating until they are nearly extinct at  $300\text{ }^{\circ}\text{C}$ .<sup>33</sup> Introduction of  $\text{O}_2$  at this temperature led to the complete disappearance of the methyl modes, indicating that the methoxy P-O bond was being broken and methanol was likely released in the gas phase.<sup>33</sup> Later studies of the decomposition of DMMP over MgO using a pulse microreactor-GC system found that methanol and formic acid evolved upon heating.<sup>34</sup> While the methoxy groups were cleaved, the C-H stretches for the methyl group did not change, indicating that the P-Me bond is never broken at room temperature.<sup>34</sup> Figure 1.8 shows the electrophilic attack of the surface on DMMP that was suggested as a likely mechanism for DMMP decomposition.<sup>33</sup> Similar results were also observed for  $\text{La}_2\text{O}_3$ .<sup>33</sup>

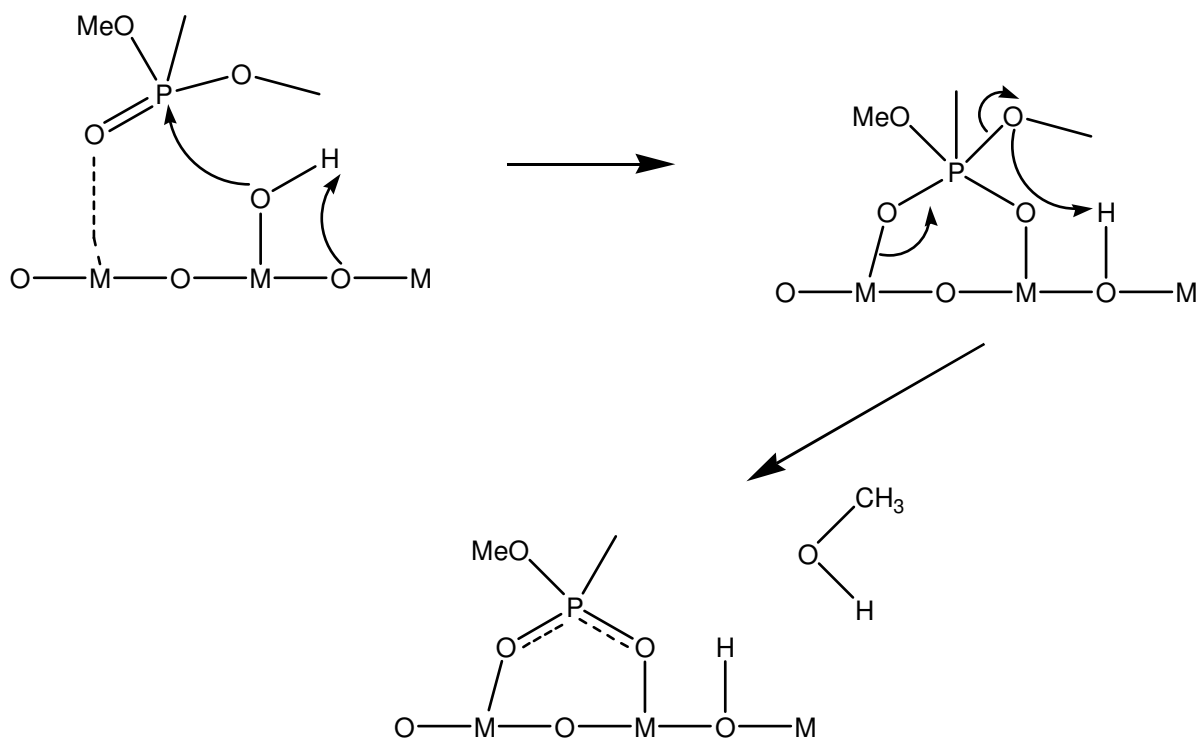


**Figure 1.8 Electrophilic attack of a metal oxide surface on using residual surface hydroxyl functionalities.**

### 1.5.2 Al<sub>2</sub>O<sub>3</sub>

The earliest work studying the interaction of organophosphorus compounds with Al<sub>2</sub>O<sub>3</sub> was performed in 1985 by Templeton and Weinburg.<sup>35</sup> DMMP adsorbs to form a physisorbed species below room temperature (200K) as observed by IR. Molecular adsorption, an interaction between a surface hydroxyl and the phosphoryl oxygen, occurs, as indicated by a red shift of the  $\nu(\text{P}=\text{O})$  peak. DMMP dissociates when the sample is heated between 273K and 473K via cleavage of the P-O bonds to form a bridging methyl methylphosphonate species.<sup>35</sup> The authors suggest the same electrophilic attack mechanism as shown in Figure 1.8.<sup>36</sup>

### 1.5.3 TiO<sub>2</sub>

Titanium dioxide has a high catalytic activity and selectivity in a wide variety of processes, such as photochemically decomposing the mustard gas simulant 2-chloroethyl

ethylsulfide (2-CEES).<sup>37</sup> Initial adsorption most likely occurs between the chlorine atom and a surface hydroxyl, followed by cleavage of the C-S bond.<sup>38</sup>

After DMMP exposure to a TiO<sub>2</sub> surface, the IR difference spectrum shows four peaks in the C-H stretching region corresponding to the asymmetric C-H methyl (3006 cm<sup>-1</sup>) and methoxy groups (2958 cm<sup>-1</sup>); and the symmetric C-H stretch of the methyl (2918 cm<sup>-1</sup>) and methoxy groups (2854 cm<sup>-1</sup>).<sup>39</sup> The  $\nu(\text{P}=\text{O})$  peak shifts upon adsorption from the condensed phase value of 1242 cm<sup>-1</sup> to 1210 cm<sup>-1</sup>, indicating that the P=O moiety loses some of its double bond character.<sup>40</sup> Two possible adsorption sites were proposed by Yates et al.: hydrogen bonding through a surface hydroxyl or the Lewis acid sites on the surface.<sup>41</sup> These acid sites could be Ti<sup>4+</sup> for the fully oxidized surface, or Ti<sup>2+</sup> or Ti<sup>3+</sup> depending on the degree of oxidation.<sup>41</sup> Raising the temperature resulted in hydrolysis of DMMP, as indicated by the growth of peaks from the bridging O-P-O species.<sup>41,42</sup>

#### 1.5.4 Fe<sub>2</sub>O<sub>3</sub>

Iron oxide shows a different reactive pathway with DMMP than other metal oxides. Mitchell et al.<sup>33</sup> exposed iron oxide to the chemical warfare agent stimulant DMMP and monitored the surface chemical functionalities formed via surface IR, and then varied the temperature to determine how reactivity changes with increasing temperature. The four peaks for the C-H stretches of methyl and methoxy moieties are present after adsorption at room temperature.<sup>33</sup> As the surface was heated, the methoxy stretching peaks decreased as observed on other metal oxides, but the methyl stretches disappear as well, signaling cleavage of the phosphorus-methyl bond.<sup>33</sup> Iron oxide is the only metal oxide that cleaves the phosphorus-methyl bond. A nucleophilic attack of

Fe<sub>2</sub>O<sub>3</sub> on DMMP has been suggested as a possible mechanism and is supported by the Mars and Van Krevelen mechanism where the iron oxide surface itself can act as a catalyst due to the low energy barrier between the multiple oxidation states of iron available.<sup>43</sup> Lattice oxygen atoms contributed to the oxidation of DMMP, providing a low energy pathway for the cleavage of the P-CH<sub>3</sub> bond.

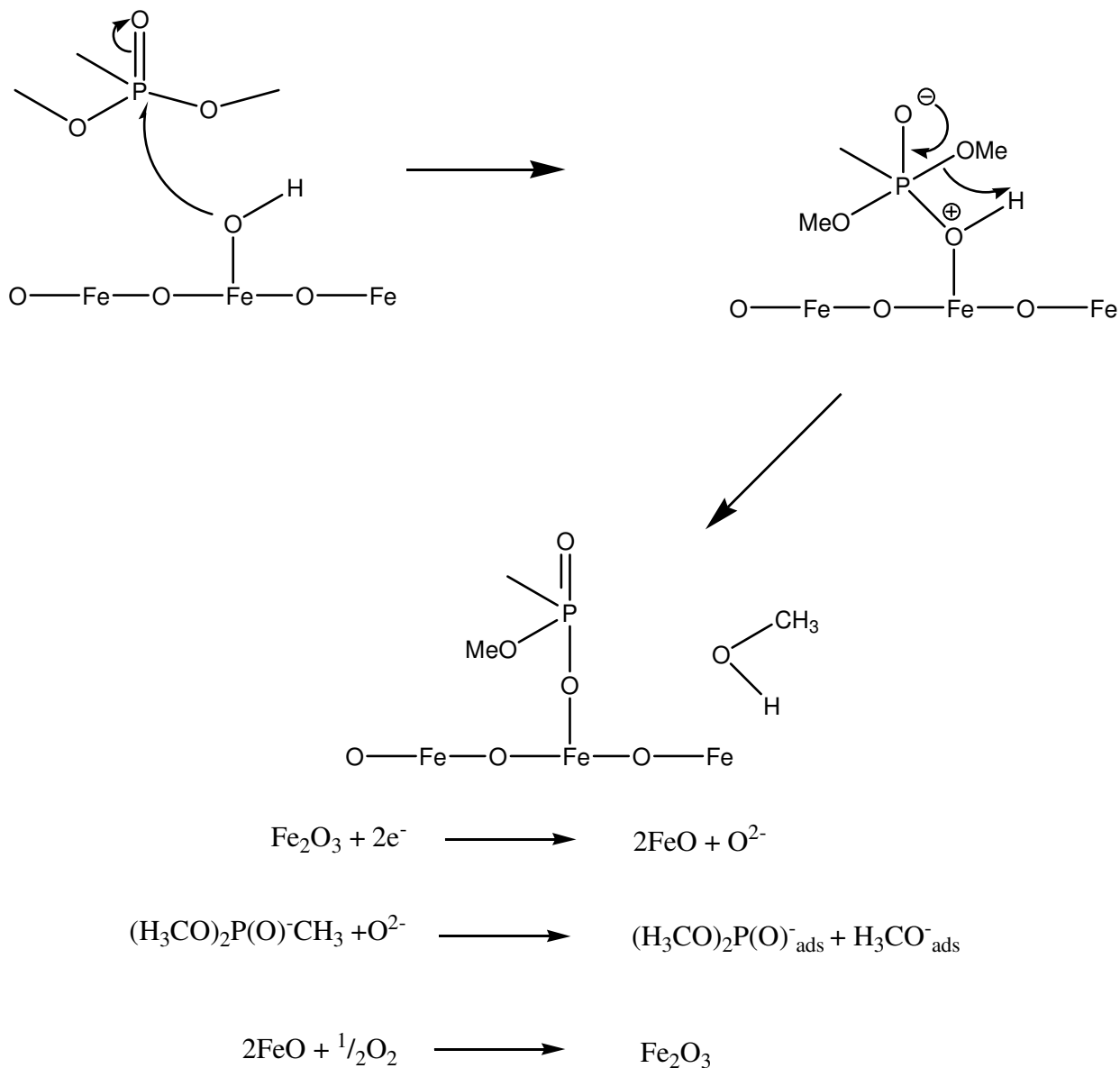


**Figure 1.9 Nucleophilic attack of the surface on DMMP and the Mars and Van Krevelen mechanism for regenerating a fully oxidized surface.**

## 1.6 Inert Gas Phase Condensation of Nanoparticles

One synthetic pathway for the formation of hafnium dioxide nanoparticles is inert gas phase condensation. If hafnium dioxide were laser vaporized under high vacuum, vapor molecules would leave the source and travel ballistically in a straight line path until they impinged on a solid surface. Because the surface is at a lower temperature than their impinging atoms, the excess energy would be lost to the substrate, leading to the growth of a homogenous thin film.<sup>44</sup> When the oxide is ablated in an inert background gas, however, the evaporated material loses kinetic energy by collisions and condenses in the gas phase to form nanoparticles.<sup>44</sup> The nanoparticles can be collected on a solid surface suspended above the bulk metal oxide pellet.

Understanding the dynamics of the evaporated material in the vapor plume is essential to controlling the size distribution and physical properties of the nanoparticles.<sup>45</sup> Okada et al. used laser spectroscopic techniques to investigate particle dynamics during nanoparticle synthesis, specifically observing at the evaporated material vapor plume. Silicon nanoparticles were created in different background gases. To visualize the plume, two-dimensional laser-induced fluorescence (2D-LIF) spectroscopy was used to trace the dynamics of atomic and molecular species,<sup>46</sup> in addition to re-decomposition LIF (ReD-LIF) to visualize clusters of atoms. In ReD-LIF, the clusters formed in the plume of evaporated material are first decomposed by a laser beam and the resulting atomic species are subsequently visible by conventional 2D-LIF. This experimental study allowed determination of the spatial distributions of atom clusters.<sup>45</sup>

When silicon is ablated in 10 Torr of helium, the resulting plume expands over time and can be captured by 2D-LIF. 200  $\mu$ s after ablation occurs, there is a decrease in

silicon density in the plume near the target silicon and the top of the plume.<sup>45</sup> When silicon is ablated in a neon background, the silicon atoms began to cluster 250  $\mu\text{s}$  after ablation. The experiment was also performed using argon, in which silicon atoms began to cluster at 300  $\mu\text{s}$ , and nitrogen, with onset at 1.2 ms.<sup>45</sup>

For the work presented in this thesis, hafnium oxide nanoparticles were synthesized using the inter gas phase condensation method. Control of the average size of nanoparticles is one of the most advantageous aspects of the gas phase condensation method. After initial size analysis, nanoparticles could be exposed to the chemical warfare agent DMMP without removing them from high vacuum with confidence that the average size was consistent with a given experimental setup. Additionally, the gas phase condensation method eliminates the need for solvents, allowing the investigation of the fundamental interactions between the nanoparticles and DMMP.

## **1.7 Hafnium Dioxide**

Hafnium dioxide has been used as a replacement for silicon dioxide as a gate dielectric<sup>47</sup> and is promising because there is a low current leakage resulting from limited electron tunneling.<sup>48</sup> Many studies involving hafnium dioxide have invoked the material as a gate dielectric for electronic purposes,<sup>49</sup> but there has been very little work using hafnium dioxide as a catalyst for organic and inorganic reactions.<sup>50</sup> Onishi et al. has shown that bulk  $\text{HfO}_2$  can oxidize carbon monoxide with a rate proportional to the carbon monoxide pressure, but independent of the oxygen pressure.<sup>51</sup> Hafnium dioxide has also been shown to decompose isopropanol<sup>52</sup> and adsorb methanol as a surface bound methoxy group.<sup>53</sup> Hafnia is also suitable for optical coatings because  $\text{HfO}_2$  thin films have a high refractive index, are UV transparent, and have high thermodynamic and

chemical stability.<sup>54</sup> Hafnium dioxide is usually an insulator, but because of defects in the cubic lattice, predominately O<sup>2-</sup> defects, an n-type semiconductor can be created by different preparation techniques. For these reasons, thin film hafnium dioxide has been used for gas sensing,<sup>55</sup> especially for carbon monoxide sensing in scheme complimentary to tin oxide.<sup>56</sup>

Because hafnium dioxide catalyzed the decomposition of isopropanol and methanol, an initial study was performed with hafnium dioxide nanoparticles in atmosphere exposed to DMMP. After exposure in a vapor deposition chamber, the nanoparticles were observed with reflection-absorption infrared spectroscopy and it was shown that the hafnium dioxide nanoparticles adsorbed DMMP. The initial studies did not provide a full understanding of the interactions with the surface functionalities or an understanding of how the various functionalities affected uptake, though they prompted the investigation presented in this body of work.

## **1.8 Conclusion**

High surface area metal oxide nanoparticles adsorb nerve agents and their simulants, including DMMP. Typically, the interaction involves the phosphoryl oxygen associating with sites on the oxide surface, followed by dissociation of the molecule, leaving a bridging O-P-O species. These studies demonstrate a need to explore other metal oxide surfaces and to identify the surface properties that are important for adsorption and decomposition. To help reach this goal, DMMP will be exposed to hafnium dioxide nanoparticles that are synthesized via inert gas-phase condensation. The gas-phase condensation method is unique because of the ability to prepare clean surfaces

that allows the basic interaction of DMMP with  $\text{HfO}_2$  to be studied in detail with surface vibrational spectroscopy.

## Chapter Two

### Experimental Approach

#### 2.1 Inert Gas Phase Condensation

Nanoparticles are considered the building blocks of nanotechnology and are often the basis of a “bottom up” approach for developing nanostructured materials and devices.<sup>57</sup> There are several liquid phase synthesis techniques for creating nanoparticles,<sup>58-60</sup> though they have interferences and contaminations from the solvent used for synthesis. Hafnium dioxide nanoparticles were synthesized by vapor phase synthesis under an inert gas background for the studies presented in subsequent chapters. The method is advantageous because the nanoparticles are synthesized in vacuum and can be transferred to the analysis chamber without exposure to atmosphere, allowing for minimization of surface contamination. In gas phase condensation, a solid pellet of hafnium dioxide is heated, in our case by a 40W cw-CO<sub>2</sub> laser, until the material vaporizes.<sup>57</sup> The vapor is cooled via collisions with the background gas, reducing the temperature of the vaporized material, resulting in a supersaturation of vapor that is thermodynamically unstable.<sup>57</sup> If the “plume” of evaporated material is sufficiently saturated, then particles will nucleate homogeneously. Therefore, in order to create smaller particles, it is desirable to have a high degree of saturation.<sup>57</sup> Subsequent depletion of material from the plume precludes formation of bulk condensed phase material. Nanoparticles created in the plume are collected on a substrate. Gold coated slides were used as substrates for exposure studies, while silicon wafers served as substrates for studies using scanning electron microscopy.

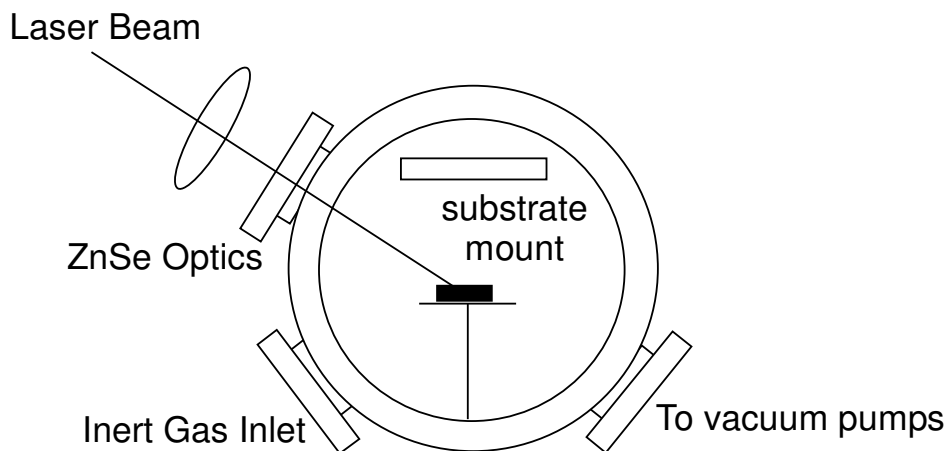


**Figure 2.1 Diagram of the inert gas phase condensation setup using a 40W CO<sub>2</sub> laser beam to ablate a bulk HfO<sub>2</sub> pellet and collect the nanoparticles on a suspended substrate.**

## 2.2 Atomic Force Microscopy

Due to the strong size dependence of particle properties, it was necessary to know particle sizes of the synthesized nanoparticles. Once the nanoparticles are created and collected, the particles are removed from vacuum, scraped off the surface, and dispersed with filtered absolute ethanol in a clean vial. The vial containing the hafnium dioxide nanoparticles and ethanol was sonicated for a minimum of ten minutes to break up aggregates and enhance particle dispersion.

A silicon wafer was cut into squares approximately 5 mm x 5 mm using a diamond glass cutter and cleaned in piranha solution for at least thirty minutes. Piranha solution is 70% concentrated sulfuric acid and 30% hydrogen peroxide by volume and is a highly oxidizing solution used to remove organic contaminants from surfaces (*WARNING: piranha solution is highly oxidizing solution that can be explosive; handle with care*). The treated and cleaned wafer was rinsed with copious amounts of deionized water, followed by ethanol, and dried in a stream of ultra high purity nitrogen. Once dried, the slide was exposed to one drop of the dilute nanoparticle solution and blown dry

immediately in a stream of nitrogen. This prevents evaporation-induced aggregation to yield a dispersed single layer, allowing for particle diameter analysis by tapping-mode atomic force microscopy (AFM). For these studies, AFM images were collected on a Veeco Multimode<sup>TM</sup> scanning probe microscope. The controller was a Nanoscope IIIa controller and a 12  $\mu\text{m}$  “E” scanner head.

Atomic Force Microscopy was first developed by Binnig in 1986,<sup>61</sup> who was able to image the lattice structure of graphite a year later.<sup>62</sup> AFM can operate on both conducting and nonconducting surfaces. A cantilever scans the solid surface while maintaining the force constant between the tip and the substrate via a feedback loop.<sup>63</sup> Tapping mode AFM was a great advance in the field because it could provide high resolution images without damaging the surface. The cantilever is oscillated while scanning across the surface and is controlled x, y, and z piezocrystals. A laser is reflected off the cantilever and is directed at the center of a photodiode detector. As the cantilever oscillates, the position of the laser changes on the photodiode. This determines the surface structure. Height analysis is used to determine nanoparticle diameter as discussed further in Section 3.2. Height is better to determine diameter because the tip has a much larger x,y cross section than the particles themselves, which is the limiting factor, creating distorted images that exaggerate the particle size in the x and y directions.

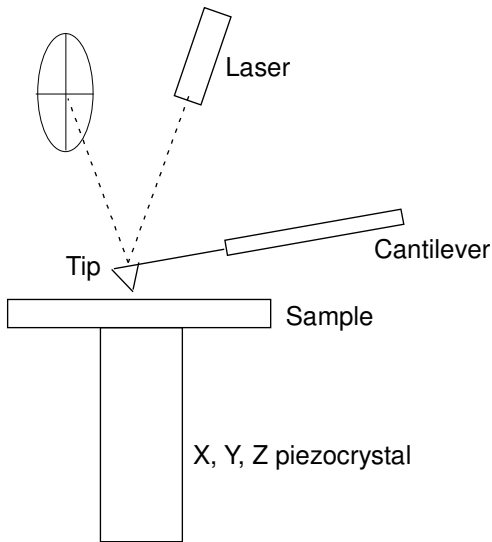


**Figure 2.2 Schematic of an AFM measurement used to analyze nanoparticles size.**

### **2.3 Scanning Electron Microscopy**

Scanning electron microscopy (SEM) is used to obtain three-dimension-like images of materials on the nanometer to micrometer scale.<sup>64</sup> One of the two major components of an SEM is the electron column, consisting of an electron gun, which generates electrons and accelerates them to energies between 100 and 30,000 electron volts, and several electron lenses that influence the path of the electrons traveling down an evacuated tube. The sample compartment at the base of the electron gun is pumped down to a pressure of approximately  $10^{-6}$  Torr. The tungsten hairpin electron generator creates an electron beam which is focused by the lenses to a smaller spot on the specimen, typically less than 10 nm,<sup>64</sup> where the electrons interact with the surface to a depth of approximately 1  $\mu\text{m}$ . The electron beam is rastered across the two dimensional surface. When the electron beam interacts with the sample, backscattered electrons and secondary electrons are collected by the Everhart-Thornley (E-T) detector, forming an image.

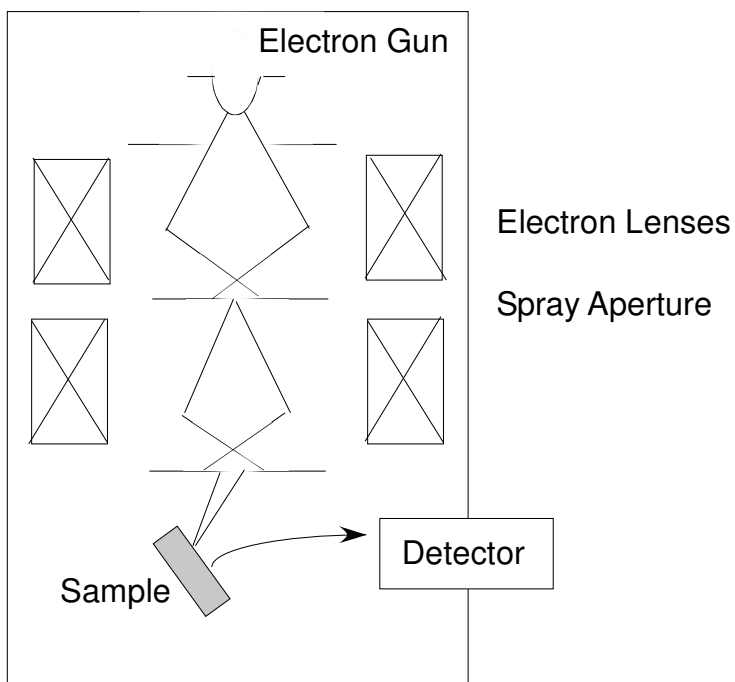


**Figure 2.3 The basic schematic of an SEM instrument.**

#### **2.4 Nanoparticle Synthesis and Ultra-High Vacuum Analysis**

Hafnium dioxide nanoparticles were synthesized in a steel chamber, as described in Section 2.1, that was directly mounted to a high-vacuum load lock chamber, which enabled direct transfer to an ultra-high vacuum (UHV) chamber. After inert gas-phase synthesis, the synthesis chamber was evacuated with a liquid nitrogen cooled sorption pump, followed by sample transfer into the load-lock chamber through a gate valve. Once the sample had been transferred, the load-lock chamber was isolated and evacuated using an ion pump until the base pressure of  $10^{-7}$  Torr was reached. A large gate valve was then opened to the main analysis chamber and the sample mount was screwed on to a threaded copper mount. This transfer procedure prevented the compromise of UHV conditions in the analysis chamber. The UHV surface analysis chamber was evacuated with an Osaka magnetically levitated turbo pump to a base pressure of  $10^{-10}$  Torr. The

sample was mounted on an x, y, z manipulator (McAllister MA1000), allowing the sample to be placed normal to the XPS hemispherical analyzer, discussed in Section 2.6, and in line with the RAIRS analytical setup, discussed in Section 2.7. Pressures were observed using a compact full range gauge (Pfeiffer PKR251).

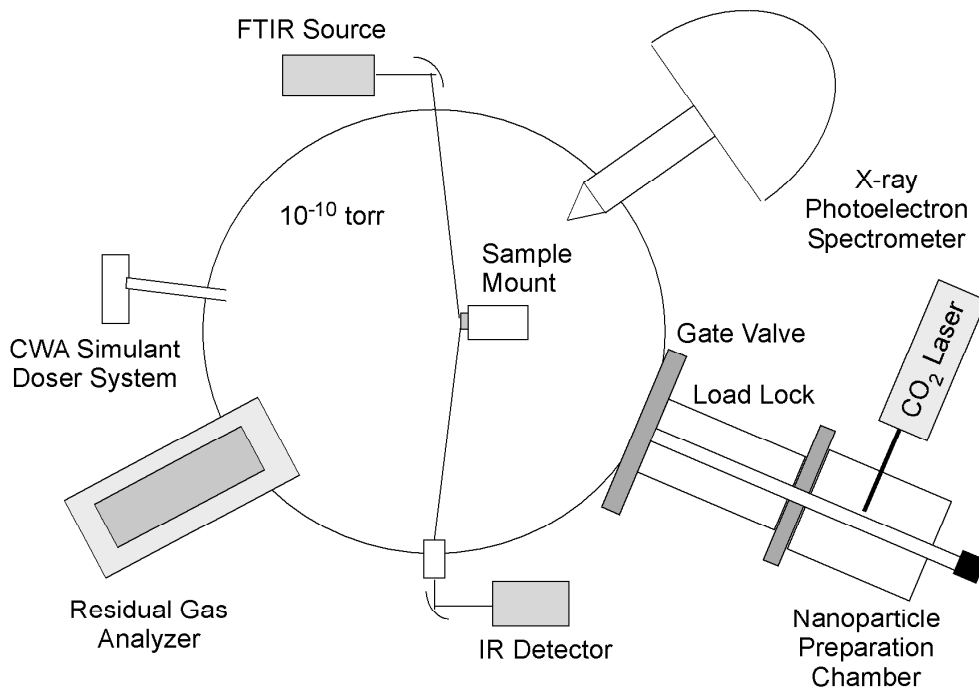


**Figure 2.4 Setup of nanoparticle synthesis with adjacent ultra-high vacuum analysis instrumentation, including RAIRS, XPS, and a residual gas analyzer.**

## 2.5 Dimethyl Methylphosphonate (DMMP) Exposure Studies

In the set of experiments presented in this thesis, DMMP was introduced into the chamber by a leak valve. An inert gas, either argon or nitrogen, was flowed through a bubbler containing several milliliters of DMMP warmed to 85°F. Some of the DMMP vapor was carried through a series of nalgene tubes to a leak valve attached to the ultra-high vacuum analysis chamber. When the valve was opened, the pressure of the chamber increased as DMMP was introduced into the chamber along with the carrier gas. The leak valve was also heated in order to minimize DMMP condensation. A quadrupole

residual gas analyzer (RGA) was used to determine the partial pressure of gases inside the main analysis chamber. The resulting mass spectrum showed residual CO<sub>2</sub>, water, nitrogen, and the carrier gas peak along with the characteristic DMMP fragmentation pattern. The base pressure of the chamber was noted prior to and after opening the leak valve. The RGA monitored the partial pressures of the background gases and used the nitrogen peak as the calibration pressure. The partial pressure of DMMP was determined by monitoring the largest peak in the mass spectrometry cracking pattern of DMMP and comparing the relative intensities of the DMMP mass spectrometry peak and the nitrogen mass spectrometry peak.

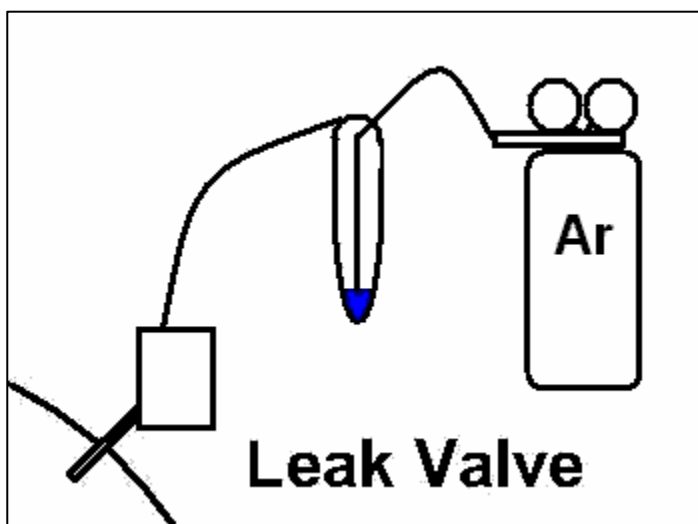


**Figure 2.6** A stream of argon bubbles through a reservoir of DMMP heated to 90°C and carried through a series of heated nalgene tubes to a heated leak valve. The leak valve was opened the main UHV analysis chamber, exposing DMMP to the HfO<sub>2</sub> nanoparticles and allowing for concurrent analysis of reactivity.

After exposure, x-ray photoelectron spectroscopy (XPS) was used to identify what chemical elements were present on the surface. In addition, XPS allowed the quantization of Hf and O present before exposure and determination of the quantity of carbon and phosphorus on the particle surface as a result of DMMP exposure. Surface

vibrational spectroscopy was used to determine the chemical functionalities on the surface before and after DMMP exposure. The combination of the two techniques allowed determination of the adsorption of DMMP and the identity of any reaction products.

## 2.6 X-ray Photoelectron Spectroscopy (XPS)

X-ray photoelectron spectroscopy was performed to determine the chemical composition of the hafnium dioxide surface. The nanoparticle sample is irradiated with photons from a Mg(K $\alpha$ ) x-ray source at 1253.6 eV.<sup>65</sup> The high energy photon strikes the sample and causes the ejection of a core level electron. To be detected, the initial energy of the x-ray must be greater than the binding energy of the core electron. After overcoming its binding energy and escaping the sample, also known as the vacuum level, the electron has some remaining kinetic energy, which is detected by the hemispherical analyzer.

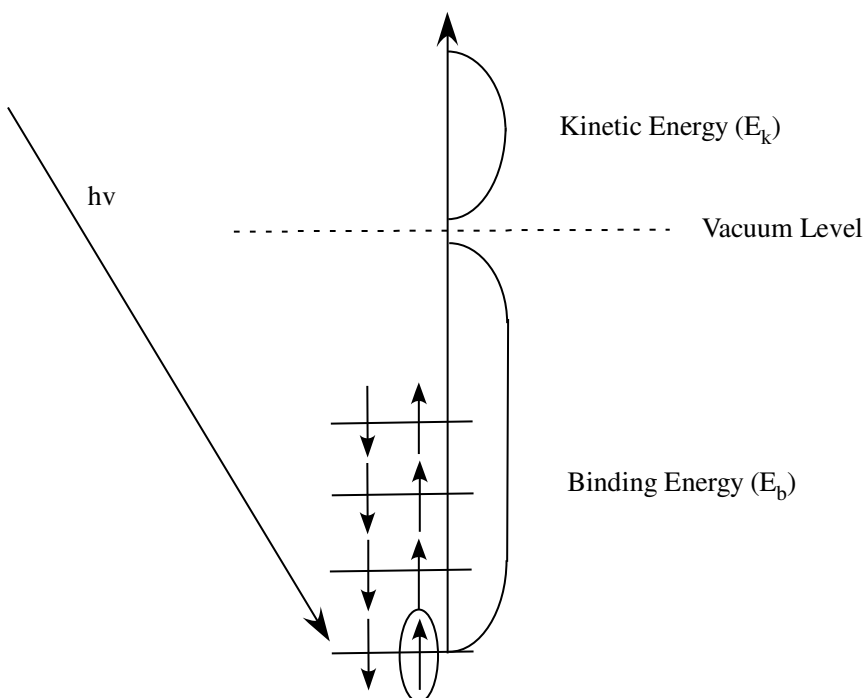


**Figure 2.6 Energy level diagrams for X-ray Photoelectron Spectroscopy.**

The binding energy of the core electron is specific for each element and is used for elemental analysis. The binding energy,  $E_B$ , is based on the incoming x-ray radiation,  $h\nu$ , and the kinetic energy,  $E_K$ , by the following equation:

$$E_B = h\nu - E_K$$

XPS experiments performed in the ultra-high vacuum analysis chamber were performed on a SPECS XR50 Mg(K $\alpha$ ) source operated at 250 W and a SPECS Phoibos 100 hemispherical analyzer. During experiments, the sample was normal to the hemispherical analyzer with an entrance slit of 7 mm x 20 mm.

## **2.7 Reflection-Absorption Infrared Spectroscopy (RAIRS)**

Studying the infrared spectrum of adsorbed species on a surface often leads to information about the identity of adsorbed species. The reflection method of IR is ideal because it avoids many of the interferences from the substrate and allows the entire IR spectral region to be used for analysis.<sup>66</sup> RAIRS will allow a study of how DMMP adsorbs on the surface and what chemical functionalities are present.

In RAIRS experiments, infrared radiation is irradiated onto the surface where the photons excite vibrations. An interferogram is collected and analyzed using Fourier Transform that results in the familiar wavelength or frequency verses absorbance plot. The main difference between RAIRS experiments and traditional IR experiments is the selection rules. The impinging IR beam has an electric field with two components: parallel to the surface, s-polarized, or perpendicular to the surface, p-polarized. After reflection on the surface, the s-polarized vector is nearly 180° from the original vector, so the net amplitude is nearly zero. Because of this, species that are parallel to the surface are typically not detected in RAIRS experiments. When the p-polarized light reflects

from the surface, the resulting vector is nearly double the original.<sup>67</sup> This is why chemical functionalities with any perpendicular component are intense in the RAIR spectrum. Greenler determined using Maxwell's Equation that the maximum signal will occur when the IR beam is impinging at  $86^\circ$  to normal. Many of the selection rules do not apply to the DMMP on hafnium dioxide nanoparticles system because nanoparticles are typically spherical. DMMP adsorbs on all sides of the nanoparticle, resulting in a wide variety of adsorbate orientations and structures. Therefore, vibrations that are usually parallel to the surface and invisible in a RAIRS experiment could be perpendicular to the IR beam if located on the side of a nanoparticle.

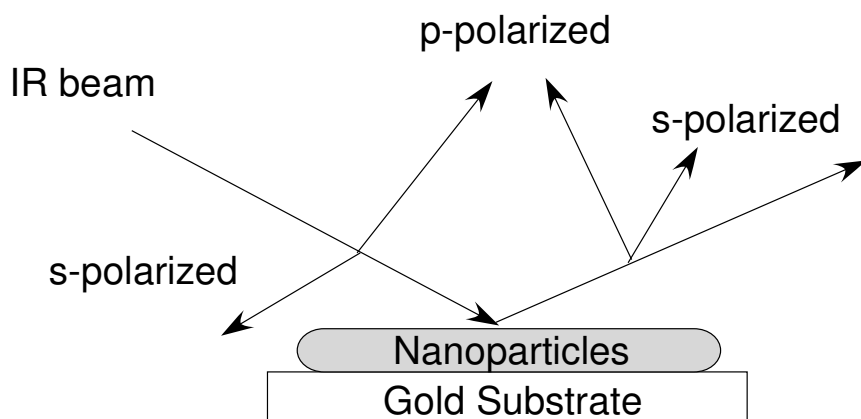


**Figure 2.7 Visual representation of electronic field vectors.**

For these experiments, a Bruker IFS 66v/S spectrometer was used with p-polarized light reflecting through the ultra-high vacuum chamber to the substrate and collected with a liquid nitrogen cooled mercury-cadmium-telluride (MCT) detector. The slit to the chamber was 2 mm and each spectrum had a resolution of  $2\text{ cm}^{-1}$  and was an average of 256 scans. Clean gold slides were used as background for the nanoparticle characterization. Once dosing started, the hafnium dioxide nanoparticles were used as the background.

## Chapter Three

### Analysis of Hafnium Dioxide Nanoparticles: Particle Size and Thin Film Morphology

#### 3.1 Introduction

Investigating metal oxide nanoparticles is important because materials on the nanoscale often exhibit different and enhanced reactivity from their bulk counterparts.<sup>21</sup> Nanomaterials also exhibit different band gap energies, melting points, and increased surface reactivity.<sup>24</sup>

Metal oxides have been used for many different catalytic applications because they exhibit both Lewis base and Lewis acid character.<sup>68</sup> Defects sites in the oxides show particularly strong acid/base properties.<sup>69</sup> Surface characteristics of metal oxides make metal oxide nanoparticles ideal substrates to study the decomposition of dimethyl methylphosphonate (DMMP). Hafnium dioxide ( $\text{HfO}_2$ ) attracts attention because of its use as a gate dielectric in electronic devices<sup>47</sup> and because it catalyzes carbon monoxide oxidation.<sup>51</sup>

#### 3.2 Experimental Setup

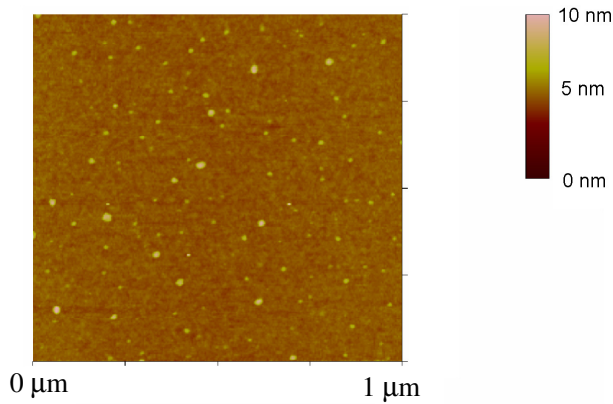
Hafnium dioxide nanoparticles were prepared by the laser ablation inert gas phase condensation method in a small, steel vacuum chamber containing a  $1 \text{ cm}^2$  gold slide mounted above a commercial sintered hafnium dioxide pellet. This chamber was first evacuated using a mechanical pump, further evacuated to high vacuum using an oil diffusion pump, and allowed to reach base pressure ( $\sim 1 \times 10^{-6}$  Torr) over two to three hours. The chamber was then isolated from the pumps and backfilled with an inert gas to a desired pressure, typically between 1 and 10 Torr. A 40 W cw- $\text{CO}_2$  laser beam was

focused to approximately a 1 mm spot on the pellet using ZnSe optics, irradiated on bulk HfO<sub>2</sub> creating nanoparticles that condensed in the gas phase and were collected.

### 3.3 Particle Size Analysis

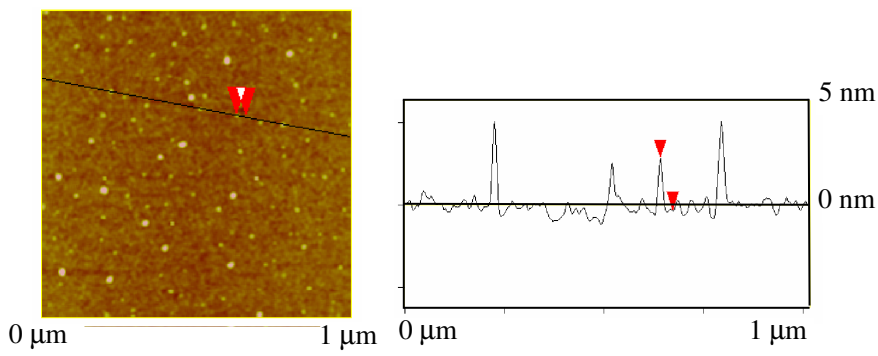
Tapping mode atomic force microscopy was used to image hafnium dioxide nanoparticles on a silicon wafer. Height mode is used to determine the average particle diameter. While this is based on the assumption that the particles are spherical, z-measurements are superior to x y-axis measurements due to tip radius induced error.

Figure 3.1 shows an example of a tapping mode AFM image of dispersed nanoparticles.



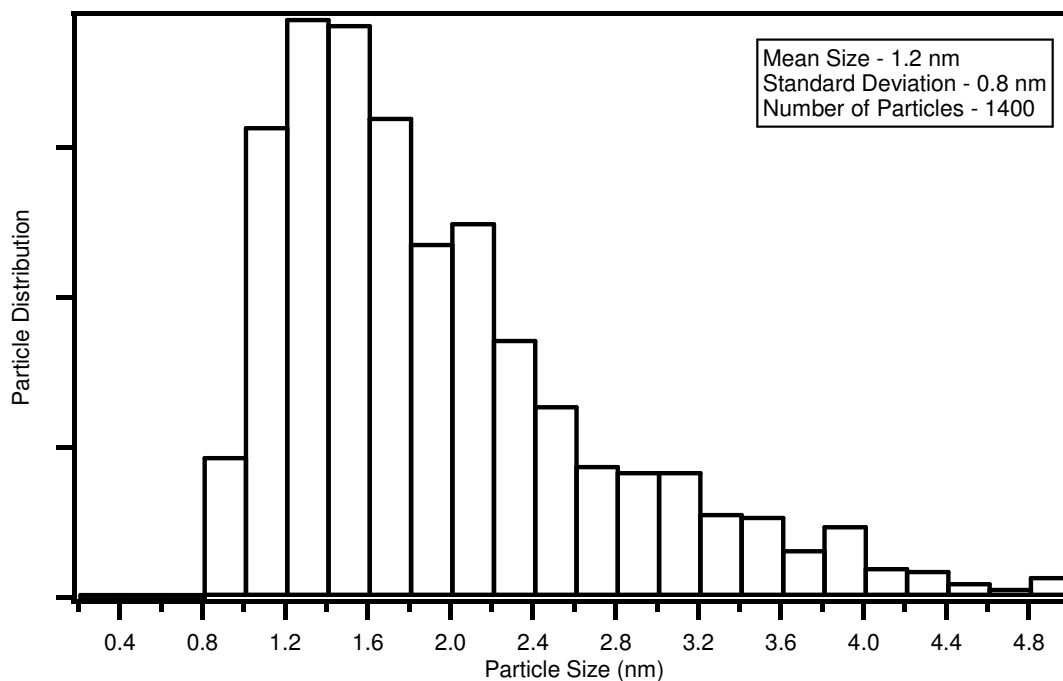
**Figure 3.1 AFM height image of a 1 μm by 1 μm area of silicon wafer with dispersed hafnium dioxide nanoparticles.**

The height scale on this image is 10 nm, as indicated by the scale bar on the right. The x and y axes are shown, while the z axis is indicated by color so that the brighter spots are imaged nanoparticles. Once a two dimensional picture has been obtained, a line is drawn across the image and a cross sectional analysis is performed.



**Figure 3.2 Cross section and height analysis for a set of nanoparticles. The difference between the arrows is the height of the nanoparticle.**

Images are collected for nine to twelve different areas on any given sample to ensure a statistical sample. The combined data is analyzed to determine an average size of particles, which is dependent on the pressure during synthesis. For particles synthesized in 1 Torr of N<sub>2</sub>, the average size was 1.2 nm ± 0.8 nm; for particles synthesized in 10 Torr of N<sub>2</sub>, an average size of 2.3 nm ± 0.8 nm was found. The distributions are shown in Figure 3.3.



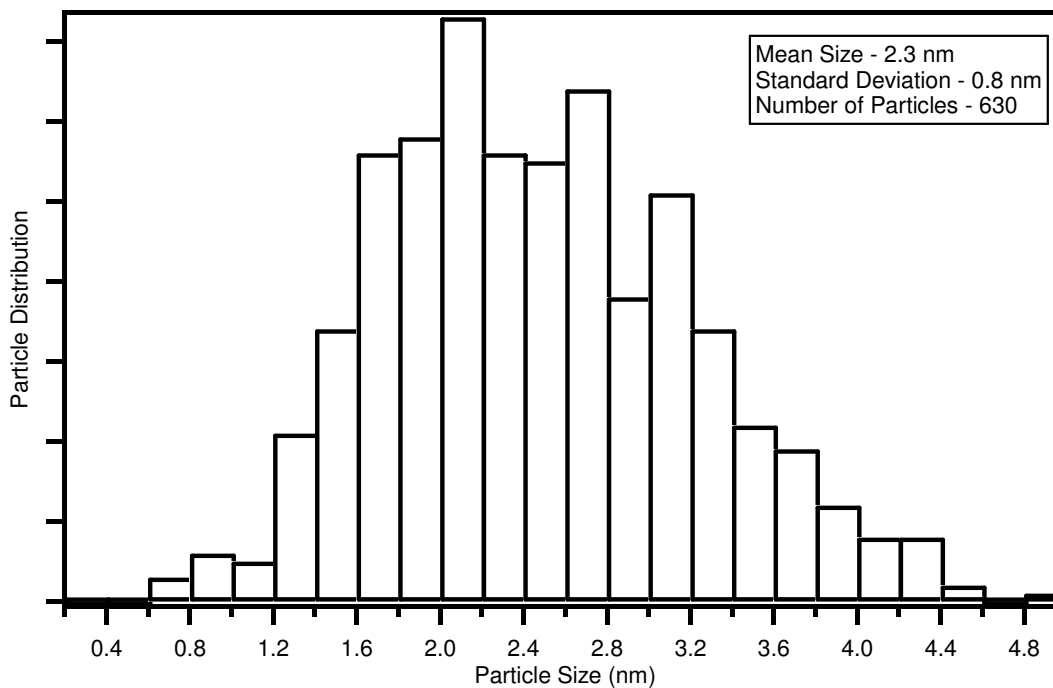


**Figure 3.3 Distribution of sizes of particles created in 1 and 10 Torr of nitrogen.**

While most of the nanoparticles used in this study were formed in nitrogen, hafnium dioxide nanoparticles were also synthesized in an atmosphere of 1 Torr of oxygen. Yates et al. suggested that defect sites, particularly oxygen defect sites, are responsible for the enhanced reactivity of nanoparticles and have shown that nanoparticles synthesized in an oxygen flux will have less oxygen vacancies than those synthesized in an inert atmosphere.<sup>70</sup> The average particle size from the AFM study is 3.2 nm with a standard deviation of 1.5 nm. There is a very broad size distribution as observed in Figure 3.4, leading to a large standard deviation.

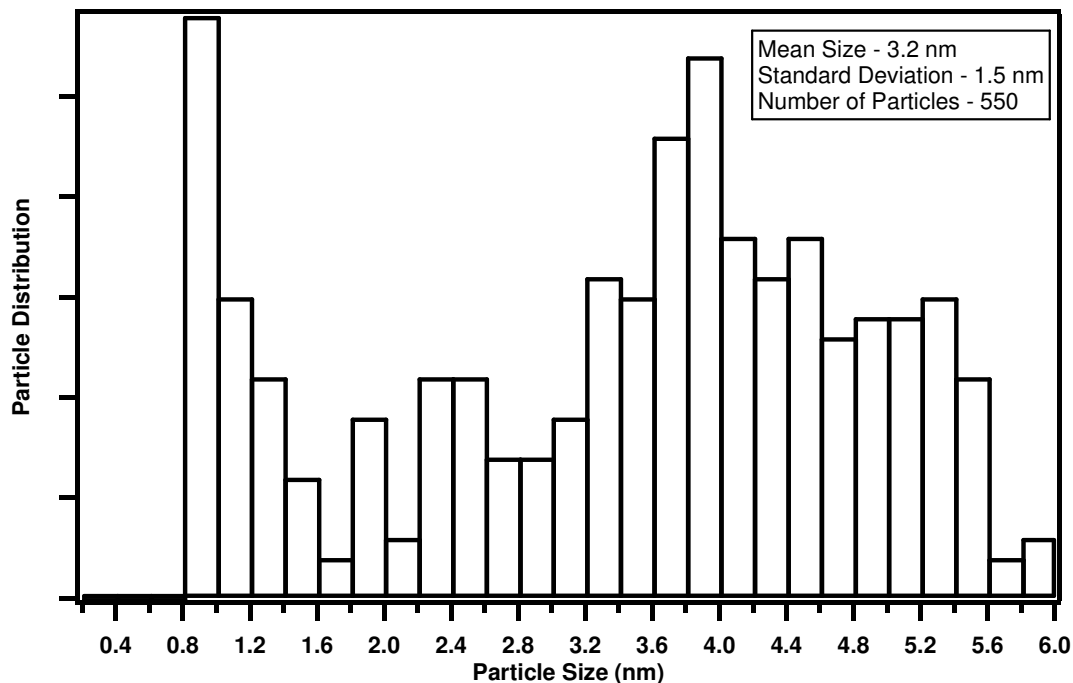


**Figure 3.4 Distribution of hafnium dioxide nanoparticle sizes when synthesized in oxygen.**

### 3.4 Microscopic Film Morphology

As a bulk hafnium dioxide pellet is ablated with the 40W cw-CO<sub>2</sub> laser, a plume of nanoparticles forms in the steel chamber. In addition to having different particle sizes, nanoparticles formed in different pressures of background gas aggregate on the surface differently. Scanning electron microscopy (SEM) was used to obtain images of as-prepared hafnium dioxide nanoparticulate films on a silicon wafer. When the particles were formed with a backfill pressure of 1 Torr, the nanoparticles formed tree-like structures on the surface. SEM images were recorded at various magnifications to observe how the morphologies are structured from the bottom up.

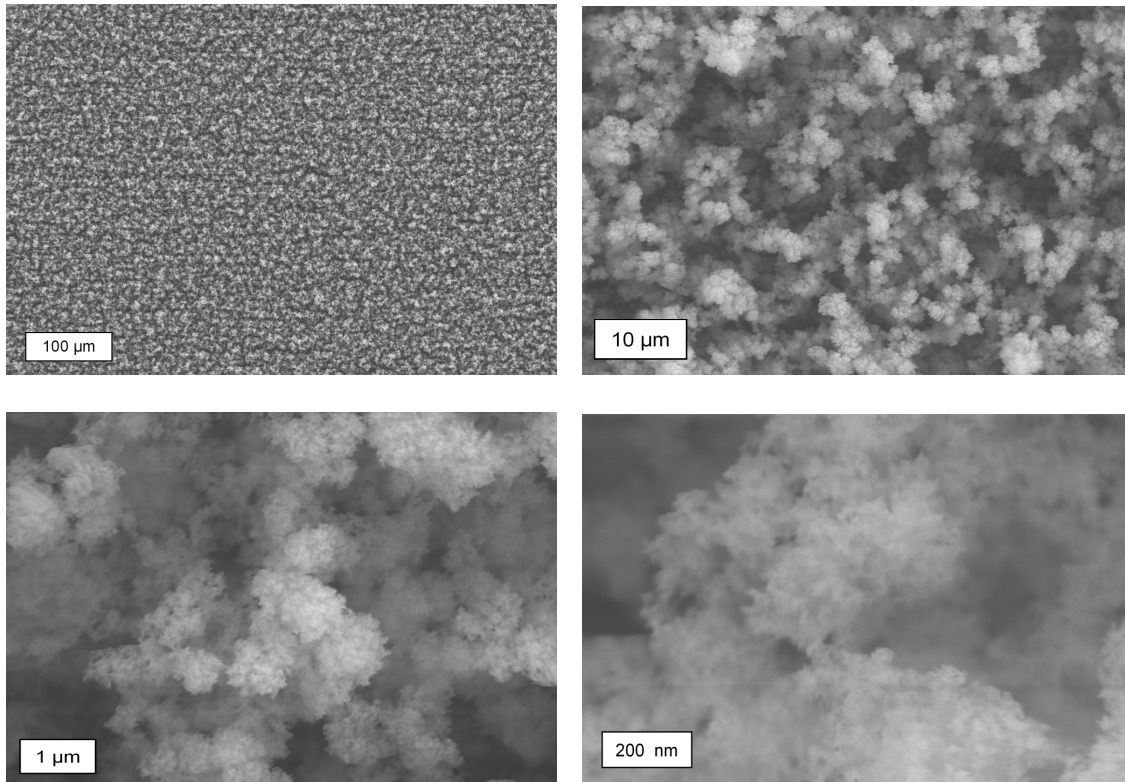


**Figure 3.5 Nanoparticle thin film morphology created in one Torr of nitrogen at 500x, 5,000x, 10,000x, and 20,000x magnifications.**

After vaporization of the hafnium dioxide pellet, a plume of gas phase hafnium dioxide arises and condenses to form nanoparticles. In a lower background pressure, the plume is larger and although particles are smaller, they can aggregate together. As seen in the highest magnification SEM image, the particle aggregates seem to be very loosely held together. These loose aggregates stick to the surface and form column-like structures.

As the pressure of the nitrogen backfill in the chamber increases, the resulting thin film on the surface changes morphology from a tree-like morphology to a web-like morphology. The nanoparticles themselves are larger and are aggregating in the plume in

chains rather than larger, loosely packed spheres, perhaps due to addition interactions with the background gas.

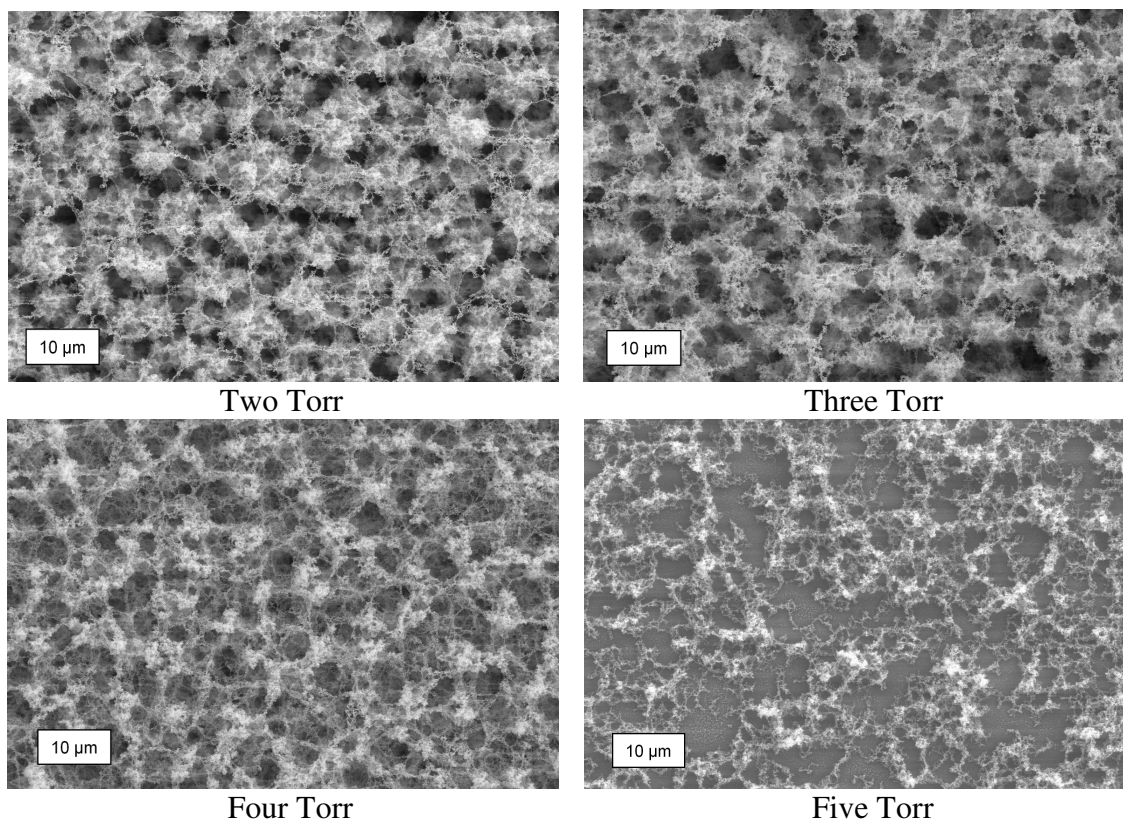


**Figure 3.6 SEM images of nanoparticles formed in 2, 3, 4, and 5 Torr of nitrogen at 5,000x magnification.**

To determine if the substrate itself had any influence on the thin film morphology, silicon wafer surfaces were functionalized with different self-assembled monolayers, creating both a hydrophilic, hydroxyl terminated surface and a hydrophobic, methyl terminated surface. Hafnium dioxide nanoparticles were created as before by the inert gas phase condensation method with a background pressure of 1 Torr. This should create the fluffy, tree-like structures seen in Figure 3.6. SEM images suggest a similar structure for films on the self-assembled monolayer as the silicon surface, suggesting the underlying substrate has little influence as to how the nanoparticles collect on the surface.

This supports the hypothesis suggested in the literature that the nanoparticles form aggregates in the gas phase before they interact with the surface.

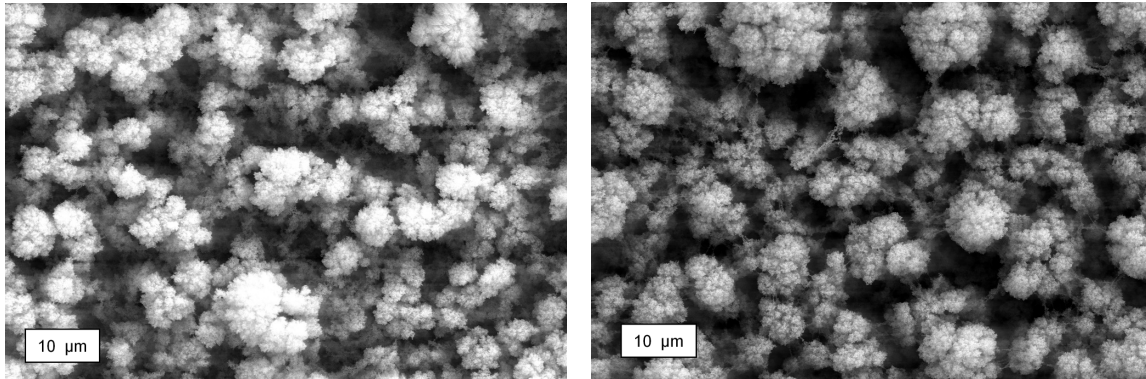


**Figure 3.7 Hafnium dioxide nanoparticles formed in 1 Torr of nitrogen on a methyl terminated, hydrophobic self-assembled monolayer surface and a hydroxyl terminated, hydrophilic self-assembled monolayer surface.**

The edge of the thin film may indicate how the first several layers of nanoparticles form on the surface. While the majority of the thin film looks like fluffy, tree-like structures, the nanoparticles closest to the silicon wafer have a web-like morphology similar to a thin film formed at higher pressures. This provides an underlying layer to the tree-like structure above.

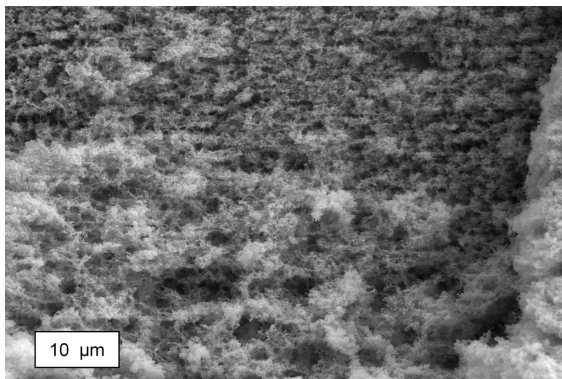


**Figure 3.8 Edge defects of the thin film formed in 1 Torr of nitrogen.**

### **3.5 Conclusion**

The different film structures observed for nanoparticles deposited under different pressures is most likely attributed to changes in the background gas. The formation of nanoparticles results from the cooling of vapor material by collisions with the background gas within the ablation plume.<sup>71</sup> Vapor material is quickly depleted after saturation-induced nucleation and growth of nanoparticles occurs, preventing excessive growth of nanoparticles. Under lower pressures, the plume is less spatially confined and cools less rapidly, resulting in isolated particles or clusters depositing on the surface; here, growth of columns is directed by attractive forces such as electrostatic interactions. Under higher pressures, the plume is more confined, resulting in a higher particle density and therefore, greater collisions probabilities.<sup>71</sup> The transport characteristics of aerosols in gases result in the formation of a web-like aggregate, which deposits on the surface. The greater density for the tree-like film is due to the directed growth, while the aggregates formed under higher pressure have a more open structure, resulting in a film with lower density.

## Chapter Four

### Reactivity of Hafnium Dioxide Nanoparticles with Dimethyl Methylphosphonate

#### 4.1 Introduction

Chemical warfare agents are a persistent threat to society today and developing practical techniques to destroy these agents is of utmost importance. The focus of decontamination techniques should be speed and ease of use, especially since the most useful application would be in the battlefield.<sup>1</sup> Understanding the interactions between a surface and the agent is extremely important for designing systems that can quickly adsorb and decompose chemical warfare agents.<sup>1</sup> Simulants for chemical warfare agents are used for most studies rather than the actual agents because they are much less toxic. Dimethyl methylphosphonate (DMMP) is a phosphonate ester and a common simulant for the chemical warfare agents sarin and soman.<sup>33,35,40,72-81</sup> The goal of this research is to understand the fundamental interactions between the chemical warfare agent simulant dimethyl methylphosphonate (DMMP) and hafnium dioxide nanoparticles.

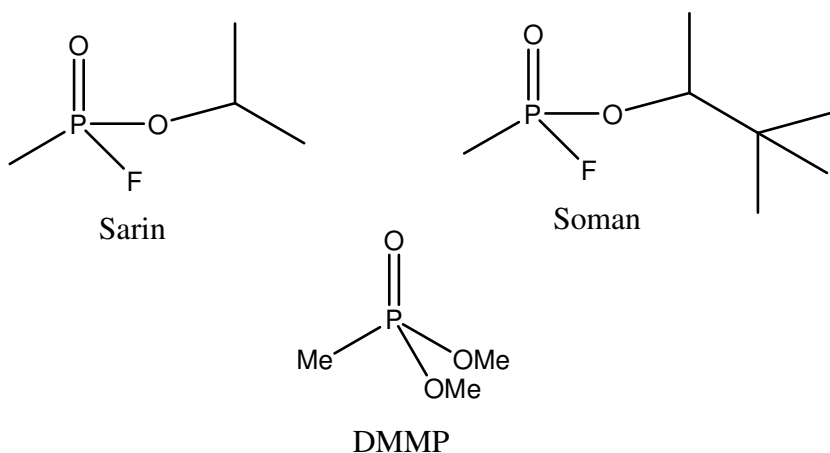


**Figure 4.1** Chemical structures of sarin, soman, and DMMP, the simulant used in this study.

## **4.2 Exposure Studies**

To expose nanoparticles to DMMP, HfO<sub>2</sub> nanoparticles are ablated on a 1 cm<sup>2</sup> clean gold slide. The gold slide is necessary because it serves as the reflective surface for infrared analysis. The freshly synthesized hafnium dioxide nanoparticles are directly transferred from the high vacuum synthesis chamber into an ultra-high vacuum analysis chamber, as described in Section 2.4.

### **4.2.1 DMMP on a Gold Substrate**

The goal of this thesis is determining how DMMP interacts with hafnium dioxide nanoparticles, so any influence of the underlying substrate must be ruled out. For this infrared study, gold is used as the background for the infrared spectra, resulting in a difference spectrum. As DMMP is exposed to the gold slide, changes in the spectra would be indicative of an interaction between the two. As a difference spectrum, negative peaks indicate chemical functionalities that are being removed from the surface. There are slight negative peaks resulting from changes in the water and CO<sub>2</sub> levels in the IR detector box and on the IR optics. Sharp peaks at 1250 and 1800 cm<sup>-1</sup> result from the turbo pump interfering with the detector. The resulting spectrum is nearly flat, indicating that DMMP has no interaction with the gold substrate.

### **4.2.2 DMMP on a Cold Gold Substrate**

Studies have shown that a self-assembled monolayer on a cold gold substrate can collect DMMP ice. Exposing DMMP to a clean gold slide cooled to -100 °C will serve to eliminate possible interactions if a nanoparticle surface is cooled and exposed to DMMP. A clean gold slide was introduced into the analysis chamber. It was cooled using a helium cryostat via a copper braid connected from the helium cryostat to the copper block

sample mount. The temperature was monitored through a thermocouple attached to the block. Approximately 140 Langmuir of DMMP was dosed onto the surface at  $-100\text{C}^{\circ}$  and the RAIR spectra monitored the development of surface bound species. According to the spectra during exposure, DMMP does not adsorb to a cold gold surface as indicated by the lack of positive spectral peaks. Therefore, if hafnium dioxide nanoparticles are cooled in future studies, any spectral changes will result from interactions with the nanoparticles and not the underlying substrate.

### 4.2.3 X-ray Photoelectron Spectroscopy Characterization

To ascertain the chemical composition of the hafnium dioxide nanoparticles, X-ray photoelectron spectroscopy (XPS) was used to perform elemental analysis on the particle film. After particles were created and transferred into the ultra-high vacuum analysis chamber, the sample was oriented normal with respect to the XPS hemispherical analyzer.

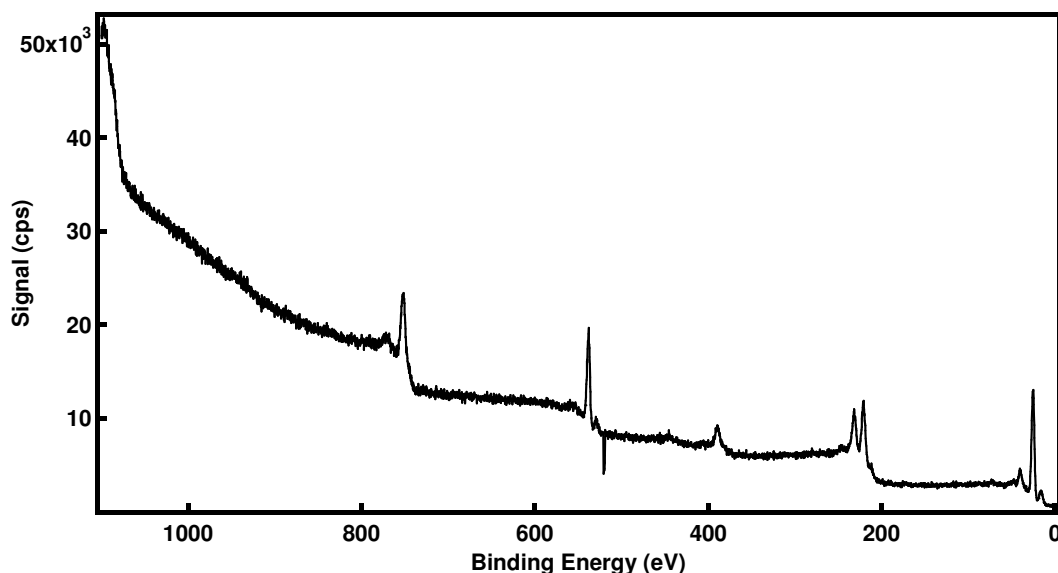


**Figure 4.2 XPS spectrum of hafnium dioxide nanoparticles before exposure to DMMP.**

It is possible to pick out the specific oxygen Auger transition at 751.1 eV. The other spectral peaks were compared to standard XPS line spectra references.<sup>82</sup> The oxygen peak corresponding to the 1s photoelectron appears at 537.8 eV and directly next to this peak is a satellite peak at 558 eV. The remaining hafnium peaks corresponding to the 4p, 4d, 5p, and 4f electrons are assigned.<sup>82</sup> No C1s is detected, indicating that organic contaminants are below the detection limit of our XPS system, ~1%.<sup>83</sup> The atomic percentages are based on the areas of the oxygen 1s peak and the hafnium 4f peak. The area of each peak is divided by the atomic sensitivity;<sup>82</sup> the relative abundances of oxygen and hafnium can then be determined. As seen in Table 4.1, the hafnium content is much higher than expected and the oxygen content is lower than expected. The nanoparticles were synthesized and transferred to the analysis chambers without atmosphere exposure, resulting in many oxygen vacancies and a much more reduced surface than expected.

Hf	Expected	33.3%
	Actual	44.6%
O	Expected	66.7%
	Actual	55.4%

**Table 4.1 Expected atomic percentages versus actual atomic percentages.**

#### **4.2.4 Infrared Characterization of Hafnium Dioxide Nanoparticles**

Nanoparticles were deposited on a gold slide in a nitrogen background pressure of 1 Torr. Using a reference spectrum of clean gold, the RAIR spectrum shows absorbances for chemical functionalities adsorbed to the surface. While these nanoparticles were ablated in high vacuum and transferred by a load lock into ultra-high vacuum, there are still several positive peaks in the IR spectrum. The most obvious peak occurs below 1000  $\text{cm}^{-1}$  and corresponds to the hafnium dioxide absorption of the IR radiation. The

peak at  $1550\text{ cm}^{-1}$  is assigned to carbonate groups bound to the nanoparticles<sup>38</sup> while the two peaks at  $3700$  and  $3800\text{ cm}^{-1}$  are associated with hydroxyl groups bound to the nanoparticles.<sup>41</sup> Uptake of background gases is not surprising because of the hydroscopic properties of high surface area metal oxides. When compared to IR spectrum of hafnium dioxide nanoparticles exposed to the atmosphere (not shown), the contaminant peaks observed on high vacuum nanoparticles are a small fraction, less than 10%, of those contamination peaks observed for saturated nanoparticles as determined by comparing relative peak intensities of the  $\text{CO}_2$  and hydroxyl surface contaminants. This leads to the conclusion that while there are some contaminants on the hafnium dioxide nanoparticles, the amount of carbonate or hydroxyl groups is very small, correlating with the lack of a C1s peak in the XPS data.

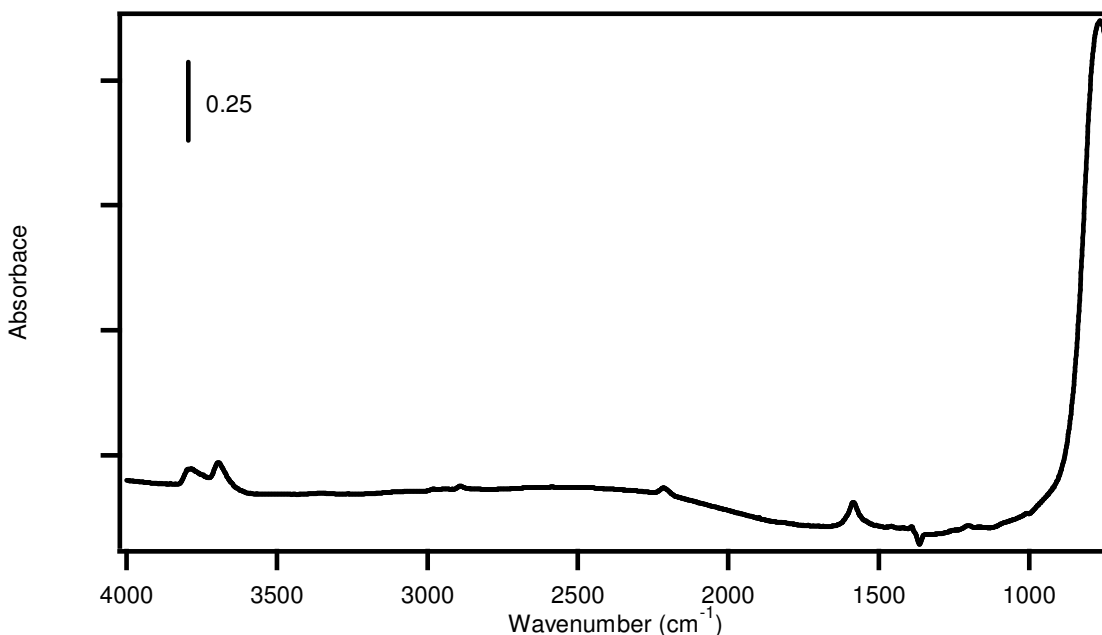


**Figure 4.3 Hafnium dioxide nanoparticles before exposure to DMMP. The high frequency peaks result from surface hydroxyl contaminants bound to two different binding sites,  $\text{CO}_2$  contaminations produce a peak at  $2200\text{ cm}^{-1}$ , surface carbonates appear near  $1600\text{ cm}^{-1}$ .  $\text{HfO}_2$  absorbs IR radiation below  $1000\text{ cm}^{-1}$ .**

#### 4.2.5 DMMP Uptake on 2.3 nm Hafnium Dioxide Nanoparticles

Once the hafnium dioxide nanoparticles have been characterized by IR, the spectrum of the particles is set as the background for subsequent data, producing a flat line. As DMMP adsorbs and reacts on the surface, the newly formed chemical functionalities are apparent by IR. When dosing DMMP, the exposure amount is represented by Langmuir (L) of exposure, where:

$$1L = 10^{-6} \text{ torr} * \text{sec}$$

One Langmuir of exposure of a particular gas would cover a  $1 \text{ cm}^2$  surface area in one second if the sticking probability were one. Assuming this, one Langmuir of exposure is approximately equal to  $5 \times 10^{14} \text{ atoms} * \text{cm}^{-2}$ .

DMMP was heated in a glass bubbler with an inert gas passing through the bubbler. The gas carried some of the DMMP vapor to a leak valve, which was opened to the main analysis chamber. RAIR spectra were obtained every five minutes for the first sixty to ninety minutes of dosing and then spectra were obtained approximately every twenty minutes thereafter. Dosing was complete when saturation was obtained, that is, when each subsequent spectrum did not exhibit noticeable change from the previous spectrum. XPS was used to determine if DMMP adsorbed on hafnium dioxide nanoparticles by comparing pre- and post- exposure surface atomic concentration. Phosphorus and carbon adsorbed on the surface signals the uptake of DMMP on  $\text{HfO}_2$ . Table 4.2 lists the atomic concentration values determined from XPS data. These results indicate that both carbon and phosphorus exist on the surface from adsorbed DMMP and the resultant products.

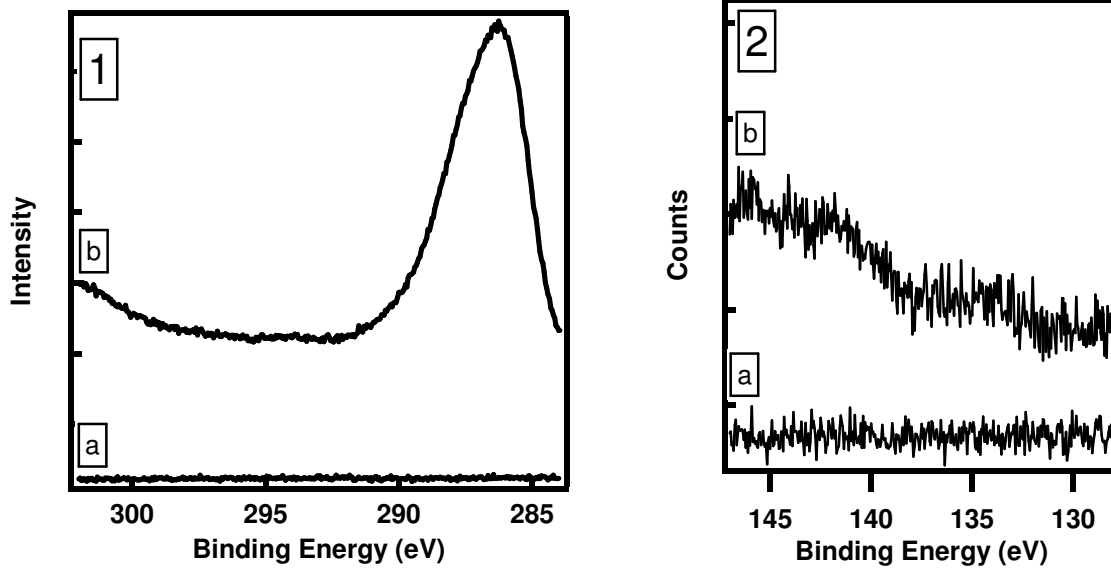


**Figure 4.4 Carbon (1) and phosphorus (2) areas of the XPS spectrum before (a) and after (b) DMMP exposure.**

Hf	47%
O	45%
C	6%
P	2%

**Table 4.2 Atomic percentages via XPS analysis after DMMP exposure.**

As DMMP was exposed to the hafnium dioxide surface, identification of surface chemical species began with comparison of RAIR spectra of gas phase DMMP and surface adsorbed DMMP.

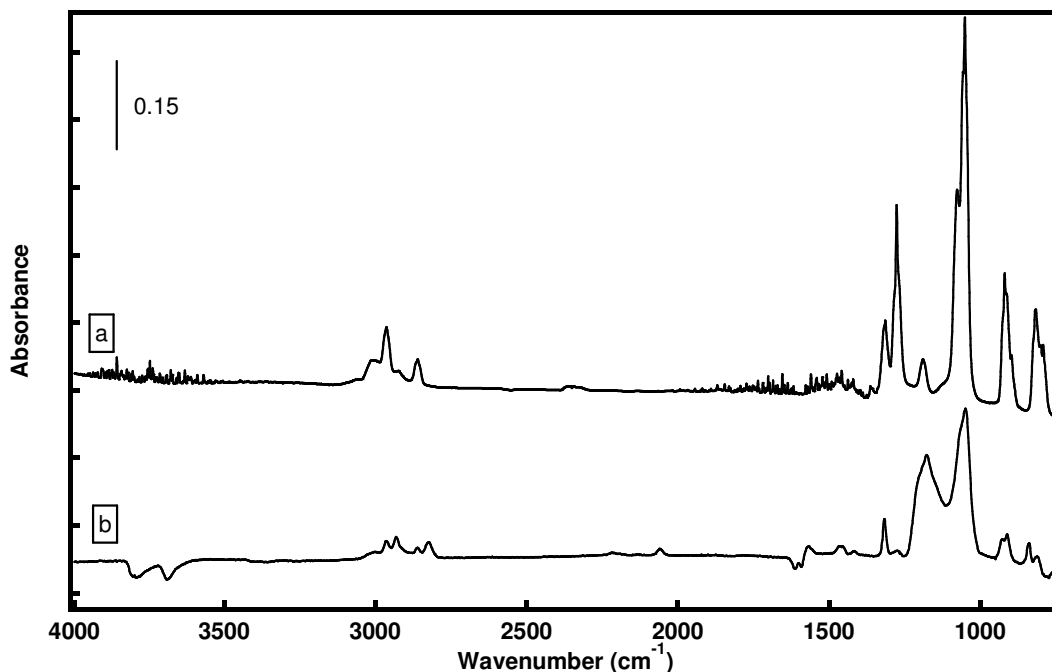


**Figure 4.5 Gas phase DMMP spectrum (a) compared to DMMP adsorbed on 2.3 nm hafnium dioxide nanoparticles (b).**

The small peaks in the baseline between 3500 and 4000  $\text{cm}^{-1}$  and 1300 and 1700  $\text{cm}^{-1}$  of the gas phase DMMP spectrum are a result of background water vapor in the instrument. By comparing the gas phase DMMP spectra, in which all of the peaks are known, one can begin to identify which chemical functionalities change upon adsorption. The first noticeable peaks for DMMP-HfO<sub>2</sub> spectrum are the two negative peaks at 3792 and 3683  $\text{cm}^{-1}$ . These are attributed to the perturbation or loss of both isolated and associated hydroxyl groups,<sup>41</sup> possibly upon initial adsorption of DMMP.<sup>39,41</sup> The high frequency C-H stretching regions contain clues about the products adsorbed on the nanoparticle surface.

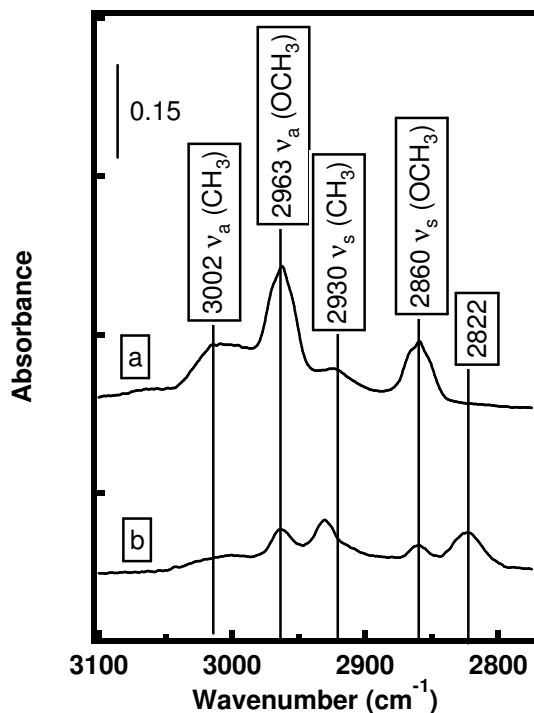


**Figure 4.6 C-H stretching region of the gas phase DMMP spectrum (a) and the spectrum of DMMP adsorbed on to hafnium dioxide nanoparticles (b).**

There are four peaks in the spectrum of DMMP adsorbed on  $\text{HfO}_2$  that correspond to the gas phase DMMP spectrum and are supported in the literature<sup>33,78,84</sup>. The highest energy peak at  $3002\text{ cm}^{-1}$  corresponds to the asymmetric stretch of the C-H bond of the methyl group, while the asymmetric C-H stretch of the methoxy group is observed at  $2963\text{ cm}^{-1}$ . The two symmetric stretches for the C-H bond of the methyl and methoxy groups occur at  $2930$  and  $2860\text{ cm}^{-1}$ , respectively. There are two peaks that do not agree with the gas phase DMMP spectrum; the first is the peak at  $2930\text{ cm}^{-1}$ , which is nearly twice the relative intensity as the corresponding peak in the gas phase DMMP spectrum. The second peak at  $2822\text{ cm}^{-1}$  is not observed in the gas phase spectrum. There are several examples in the literature of DMMP decomposition on metal oxide surfaces at elevated temperatures that report a breaking of one of the P-O bonds of a methoxy group to form methanol that is released from the surface<sup>33,36</sup> or a surface bound methoxy

group.<sup>40,74</sup> Klabunde et al. also speculated that trace amounts of water in the system aided in the overall reaction, including surface bound methanol adsorption.<sup>74</sup> Methanol was later exposed to hafnium dioxide nanoparticles to confirm peak assignments (see Section 4.2.7).

Sheppard et al. exposed bulk HfO<sub>2</sub> to methanol and observed peaks in the IR spectrum at 2950 and 2825 cm<sup>-1</sup> corresponding to the asymmetric and symmetric C-H stretches, respectively.<sup>53</sup> The assignment of the symmetric C-H stretch of methanol adsorbed on HfO<sub>2</sub> is very close to the fifth peak observed in this study at 2822 cm<sup>-1</sup>. The increased intensity of the peak at 2930 cm<sup>-1</sup> relative to the gas phase spectrum may be due to the C-H stretch of the surface bound methoxy group. We propose that DMMP is adsorbing and decomposing on HfO<sub>2</sub> to form a bridging O-P-O species and a surface bound methoxy group. Further evidence can be found in the lower frequency spectrum.

Differences between the spectra of gas phase and adsorbed DMMP also appeared in the low energy region. Several peaks shift from their position in the gas phase spectrum or do not appear. The peak at 1316 cm<sup>-1</sup> in the DMMP on hafnium dioxide spectrum shown in Figure 4.7 directly correlates to peaks in the gas phase spectrum corresponding to the symmetric bend of the methyl group of DMMP. The 1316 cm<sup>-1</sup> peak does not significantly shift when DMMP is adsorbed onto hafnium dioxide nanoparticles, correlating with the unperturbed C-H stretches, implying that the methyl group is likely not involved in the adsorption process. In contrast, a large red shift is observed for the  $\nu(\text{P}=\text{O})$  mode from 1273 cm<sup>-1</sup> in the gas phase spectrum to 1205 cm<sup>-1</sup> upon adsorption, indicative of a strong interaction between the nanoparticles and the

phosphoryl oxygen. Similar results have been observed when DMMP is adsorbed on  $\text{WO}_3$ ,<sup>39</sup>  $\text{TiO}_2$ ,<sup>39</sup>  $\text{Pt}(111)$ ,<sup>85</sup>  $\text{Al}_2\text{O}_3$ ,<sup>79</sup>  $\text{MgO}$ ,<sup>33</sup>  $\text{La}_2\text{O}_3$ ,<sup>33</sup> and  $\text{Fe}_2\text{O}_3$ .<sup>33</sup>

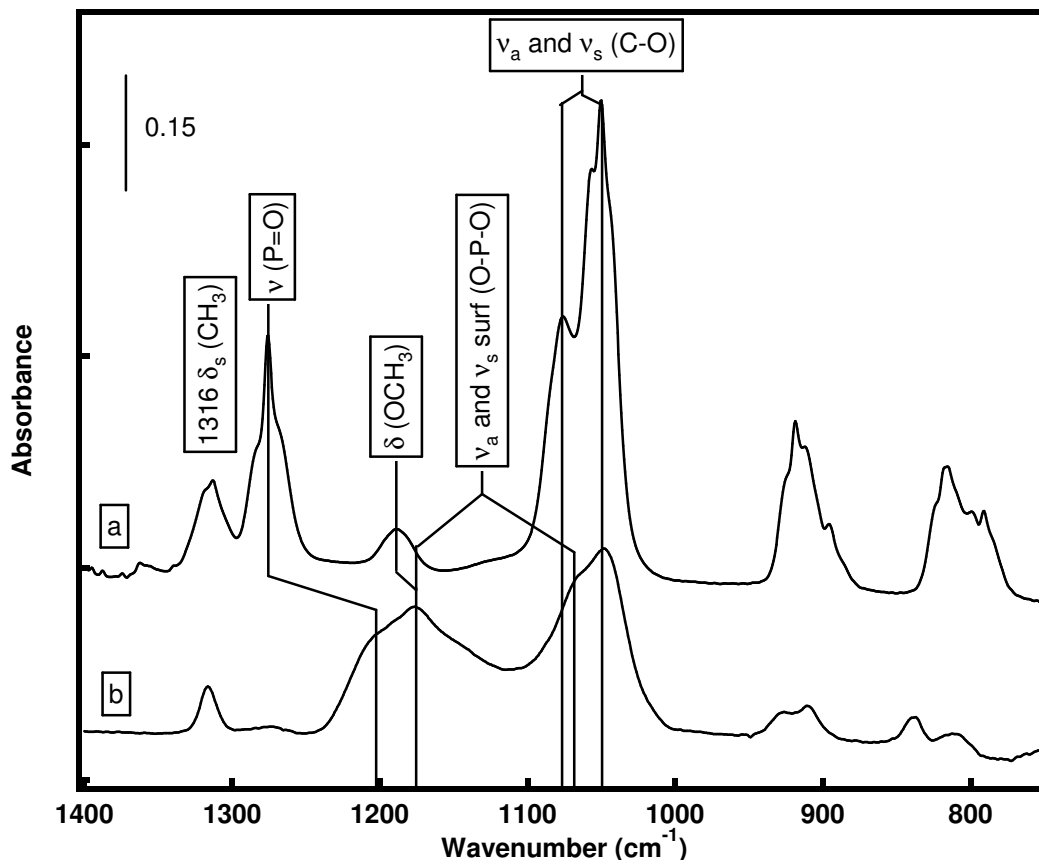


**Figure 4.7** Lower frequency region of the gas phase DMMP (a) and DMMP adsorbed on  $\text{HfO}_2$  spectrum (b).

The  $\text{OCH}_3$  deformation band shifts from  $1190\text{ cm}^{-1}$  in the gas phase DMMP spectrum to  $1177\text{ cm}^{-1}$  when DMMP is adsorbed onto hafnium dioxide where it overlaps with the peak from the asymmetric stretch of the O-P-O bridging species. This shift to lower energy has been previously reported in the literature for DMMP adsorbed on  $\text{TiO}_2$ ,<sup>78</sup>  $\text{Al}_2\text{O}_3$ ,<sup>33</sup>  $\text{MgO}$ ,<sup>33</sup> and  $\text{La}_2\text{O}_3$ .<sup>33</sup> After adsorption, the C-O asymmetric and symmetric stretches are still visible in the IR spectrum, but overlap in energy with peaks assigned to the bridging O-P-O species. The methyl rocking mode is still visible at  $1316\text{ cm}^{-1}$ , also indicating that the methyl group is not involved in the initial adsorption.<sup>39</sup>

Three important peaks lead to conclusions about the ultimate fate of DMMP on the hafnium dioxide surface. The first is the peak at  $1205\text{ cm}^{-1}$ , which corresponds to the phosphoryl oxygen stretching mode after adsorption to a surface.<sup>41</sup> This is likely due to DMMP that has adsorbed to a surface, but has not decomposed. The shift to lower energy indicates that the P=O bond has lost some of its double bond character and gains more single bond character.<sup>39</sup> The two peaks at  $1176$  and  $1070\text{ cm}^{-1}$  correspond to the asymmetric and symmetric stretches of a bridging oxygen-phosphorus-oxygen species on a surface. Kuiper et al. adsorbed DMMP on  $\gamma$ -alumina and identified the asymmetric and symmetric modes for a surface bound O-P-O species and falling within the range of  $1000$  and  $1300\text{ cm}^{-1}$  with a typical separation of  $100\text{ cm}^{-1}$ .<sup>42</sup> The separation of these peaks on hafnium dioxide is  $106\text{ cm}^{-1}$ , giving confidence to the peak assignment.

#### **4.2.6 Methanol Exposure to 1.2 nm Hafnium Dioxide Nanoparticles**

One of the suspected products of DMMP adsorption on hafnium dioxide nanoparticles is a surface bound methoxy group. Previous studies have shown that methanol exposed to a hafnium dioxide surface will result in a methoxy group bound to the surface.<sup>53</sup> If features of the DMMP exposed to  $\text{HfO}_2$  closely resemble methanol exposed to  $\text{HfO}_2$ , then the hypothesized reaction products may be confirmed. Figure 4.8 shows the C-H region of the RAIR spectrum of  $\text{HfO}_2$  nanoparticles exposed to methanol. The two peaks at  $2934$  and  $2826\text{ cm}^{-1}$  correspond to the asymmetric and symmetric stretches of the C-H bond of the methoxy group.<sup>53</sup>

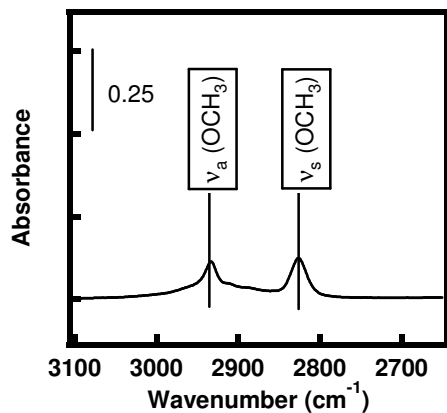


**Figure 4.8 High frequency region of methanol adsorbed on 1.2 nm hafnium dioxide nanoparticles.**

The peak shown in Figure 4.9 at  $1176\text{ cm}^{-1}$  corresponds to the rock of the  $\text{OCH}_3$  group bound to the surface and the peak at  $1053\text{ cm}^{-1}$  results from the symmetric stretch of the C-O bond of the surface bound methoxy group.<sup>53</sup> These peak results very closely correspond to several peaks in the DMMP adsorbed on hafnium dioxide nanoparticle spectrum, confirming that surface bound methoxy is a decomposition product.

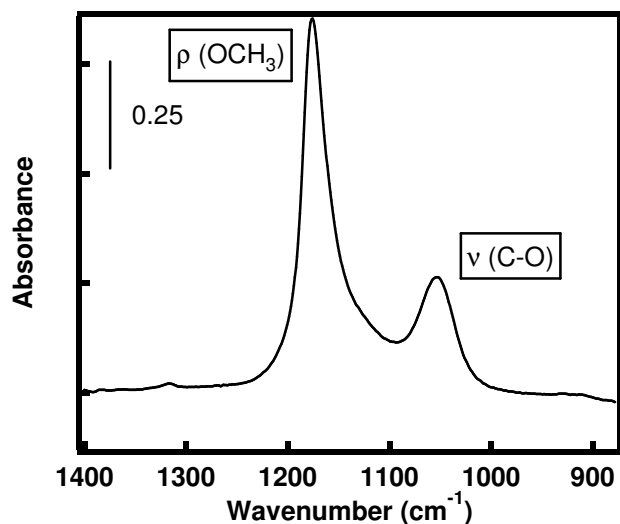


**Figure 4.9 Low frequency region of methanol adsorbed on 1.2 nm hafnium dioxide nanoparticles.**

#### 4.2.7 TMP Exposure to 1.2 nm Hafnium Dioxide Nanoparticles

To supplement peak assignments described above, 1.2 nm hafnium dioxide nanoparticles were exposed to trimethyl phosphonate (TMP). This is structurally similar to DMMP, but does not have a methyl group and will aid in the confirmation of peak assignments in the high frequency C-H stretching region.

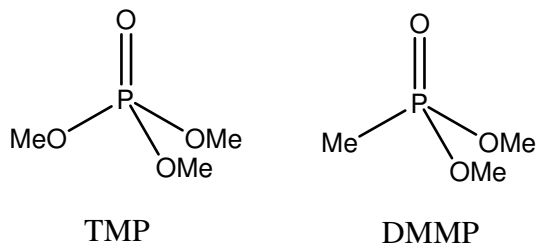


**Figure 4.10 Structures of TMP and DMMP.**

The peaks at 2934 and 2828  $\text{cm}^{-1}$  in Figure 4.12 result from the asymmetric and symmetric C-H stretches of a surface bound methoxy group. These values are very close to the stretches observed at 2934 and 2826  $\text{cm}^{-1}$  in the previous experiment of methanol on hafnium dioxide that correspond to a surface bound methanol. Two peaks at 2964 and 2861  $\text{cm}^{-1}$  are attributed to the asymmetric and symmetric C-H stretches on the bridging oxygen-phosphorus-oxygen bridging species on surface adsorbed TMP. These peaks have also been observed when TMP is exposed to  $\text{TiO}_2$ <sup>39</sup> and in theoretical work<sup>86</sup> with the same assignment. This TMP study confirms the high frequency assignments of the methyl C-H stretched of DMMP adsorbed on hafnium dioxide nanoparticles.

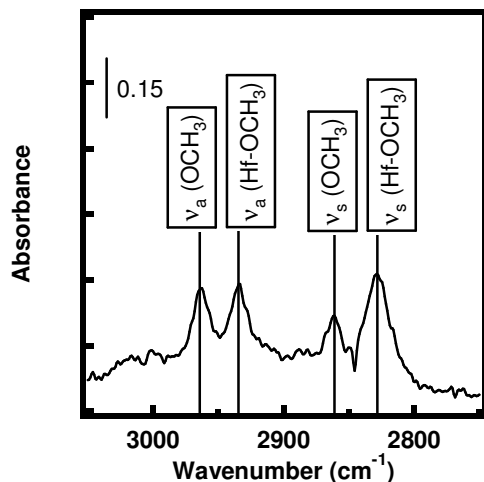


**Figure 4.11 High frequency spectrum of TMP on 1.2 nm hafnium dioxide nanoparticles.**

The lower frequency area of the spectrum in Figure 4.12 provides further evidence for decomposition of TMP on hafnium dioxide. The strong negative peak at  $1265\text{ cm}^{-1}$  results from background noise from the turbo pump. According to literature,<sup>39,87</sup> a peak at  $1266\text{ cm}^{-1}$  would indicate the P=O stretch of DMMP that had physisorbed to the hafnium dioxide surface.<sup>86</sup> In the spectrum in Figure 4.12, the peak appears at  $1245\text{ cm}^{-1}$  and is very small, indicating that most of the TMP has dissociated and formed a bridging oxygen-phosphorus-oxygen species. In the literature,<sup>39,88</sup> the methoxy rock for adsorbed TMP typically appears at  $1186\text{ cm}^{-1}$ , but in this study the rock appears red shifted at  $1158\text{ cm}^{-1}$ , likely due to a greater contribution of  $\rho(\text{OCH}_3)$  from surface bound methoxy group. These IR results indicate a substantial amount of TMP is dissociated on the surface.

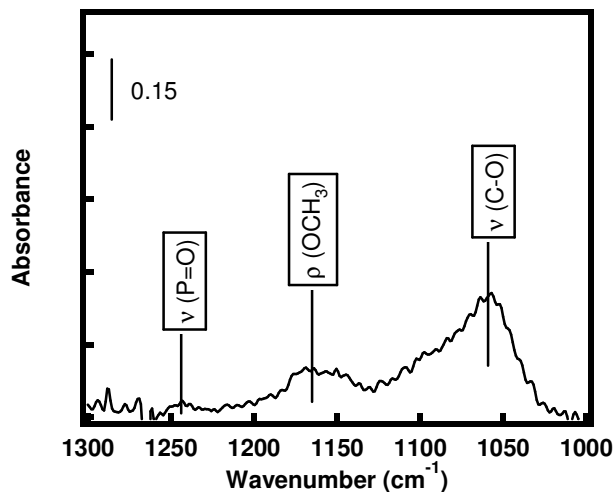


**Figure 4.12** Low frequency spectrum of TMP on 1.2 nm hafnium dioxide nanoparticles.

#### 4.2.8 Deuterated DMMP on 2.3 nm Hafnium Dioxide Nanoparticles

To support peak assignments, the methoxy groups of DMMP were deuterated according to a previously published procedure.<sup>35</sup> The assignments of deuterated DMMP on hafnium dioxide were based on previous exposures using deuterated methanol adsorbed on nanoparticles performed in the Morris lab and in the literature.<sup>35,88</sup>

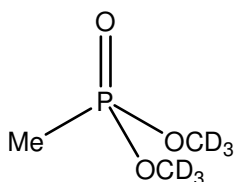


**Figure 4.13** Deuterated DMMP.

The spectrum after exposure is similar to many of the previous difference infrared spectra of DMMP on hafnium dioxide nanoparticles. In the high frequency region, the five peaks as noted before are seen, indicating that not all of the DMMP was deuterated. DMMP still underwent a surface reaction to form a bridging O-P-O species and a surface bound methoxy group on the metal oxide surface. The C-D stretches are observed at a

slightly lower wavenumber that corresponds to the isotope shift for hydrogen versus deuterium.

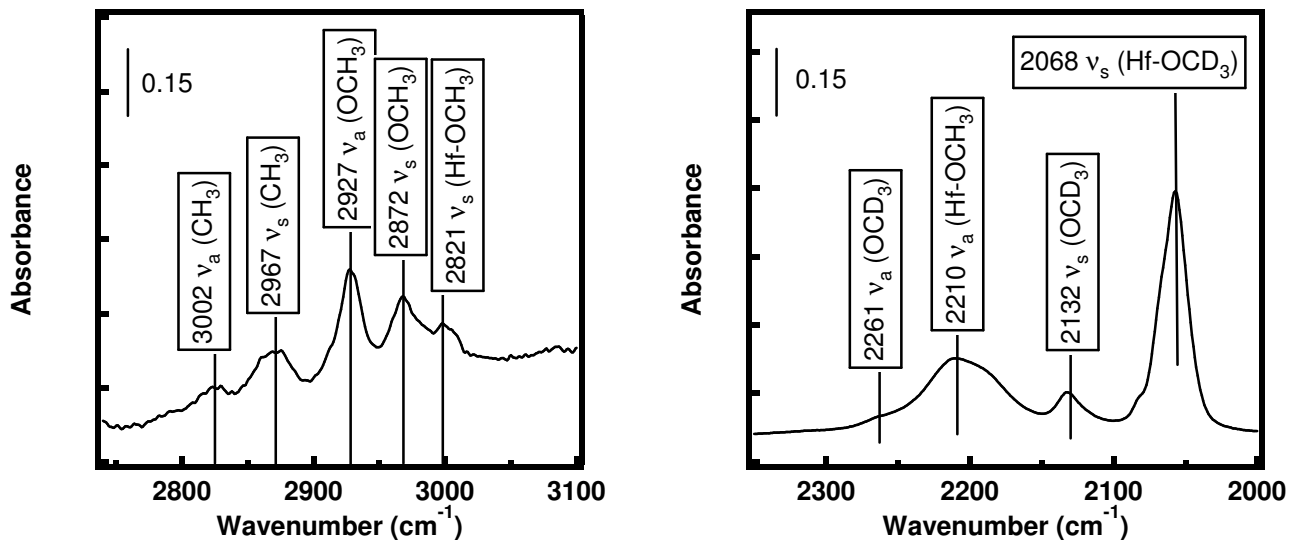


**Figure 4.14 High frequency C-H and C-D stretching region of deuterated DMMP on 2.3 nm hafnium dioxide nanoparticles. Notice that there are some undeuterated methoxy groups seen in the IR spectrum.**

The asymmetric and symmetric stretches of the phosphorus bound methoxy group are present at 2261 and 2132 cm<sup>-1</sup>. The stretches, due to the deuterated surface bound methoxy group, appear at 2210 and 2058 cm<sup>-1</sup> for the asymmetric and symmetric stretches, respectively. The lower wavenumber (not shown) region agrees well with O-P-O splitting and methyl assignments described earlier in this chapter. The products are a bridging O-P-O species and a surface-bound deuterated methoxy group as shown in Figure 4.15.

#### 4.2.9 Surface Bound Products

Figure 4.15 illustrates the two species observed on the surface after exposure to DMMP. The presence of a physisorbed species, where DMMP interacts with the surface through hydrogen bonding to surface hydroxyl groups, is supported by RAIRS data and

literature comparison.<sup>38, 41</sup> The second is a chemisorbed species, in which one of the phosphorous-oxygen bonds of the methoxy group has broken and created a surface bound methanol with a bridging O-P-O surface-bound product.

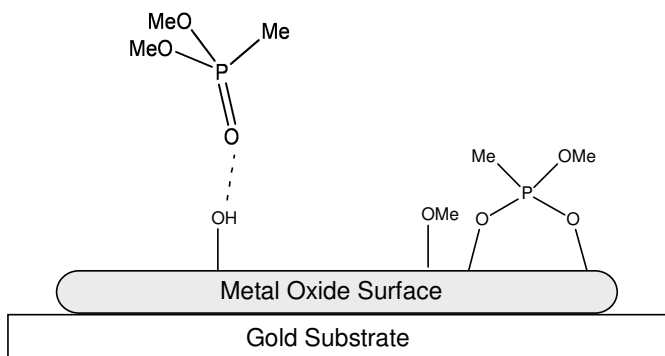


**Figure 4.15 Two different fates of DMMP on a hafnium dioxide surface.**

Once the two different species have been identified, it is desirable to determine the relative concentration of each species on the surface. The ratio of products can yield a measure of the reactivity and provide insight into the source of reactivity. Using the time dependent spectra of DMMP on hafnium dioxide, the relative amount of physisorbed and chemisorbed DMMP for any given exposure of DMMP can be determined. Figure 4.16 shows a series of RAIR spectra of  $\text{HfO}_2$  nanoparticles exposed to DMMP over time. The intensities for the physisorbed ( $1210 \text{ cm}^{-1}$ ) and chemisorbed ( $1175 \text{ cm}^{-1}$ ) peaks have similar intensities for early exposures. The immediate appearance of the chemisorbed species indicates that either dissociative adsorption occurs or that decomposition is very facile. As DMMP continues to bombard the surface from thirty Langmuir to one hundred thirty Langmuir, the chemisorbed DMMP peaks grow in intensity much faster than the physisorbed DMMP peak, indicating that DMMP already adsorbed to the surface is undergoing a surface reaction after adsorbing to the surface.

The reason for this delayed reaction is not fully understood, but is likely due unreacted DMMP migrating across the surface to more highly reactive sites.

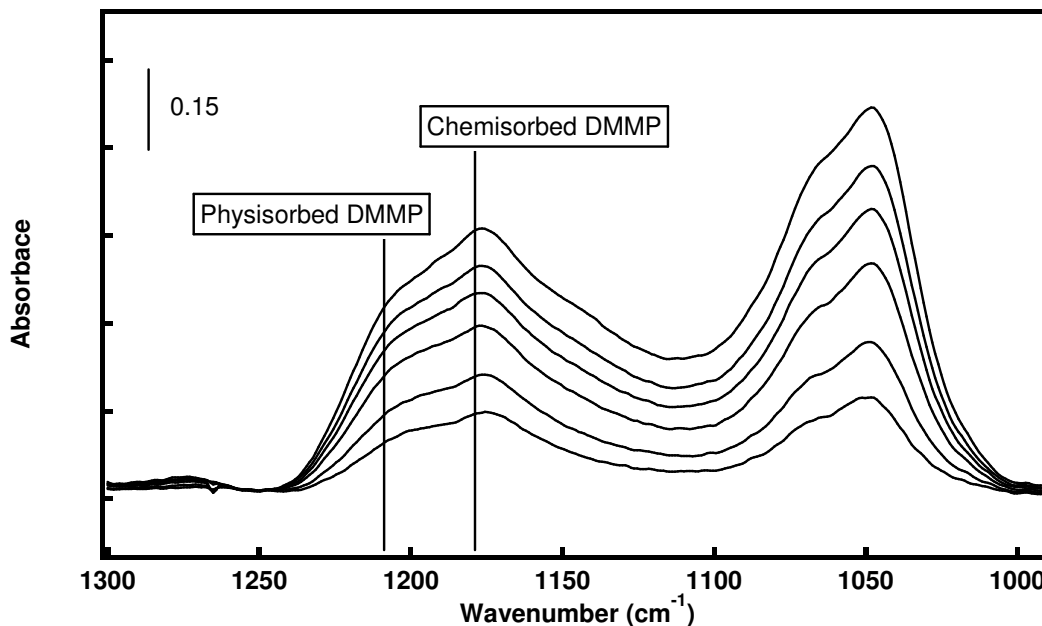


**Figure 4.16** Time dependent spectra as a function of exposure varying from 30 Langmuir to 130 Langmuir.

#### 4.2.10 DMMP on 1.2 nm Hafnium Dioxide Nanoparticles

As discussed in Section 3.2, the average size of the nanoparticles decreases to 1.2 nm if they are created in 1 Torr of nitrogen instead of 10 Torr. By decreasing the diameter of the hafnium dioxide nanoparticles, the surface area to volume ratio increases significantly, increasing the percentage of edges, which are defect sites, and are hypothesized to be highly reactive.<sup>41,70</sup> DMMP was exposed to the smaller hafnium dioxide nanoparticles to ascertain any influence of particle size on reactivity. Comparison of the spectra of DMMP adsorbed to 1.2 nm HfO<sub>2</sub> particles and gas phase DMMP shown in Figure 4.17 show peaks corresponding to the decomposition of DMMP on the surface, such as a surface methoxy group and an oxygen-phosphorus-oxygen bridging species.<sup>39,41</sup>

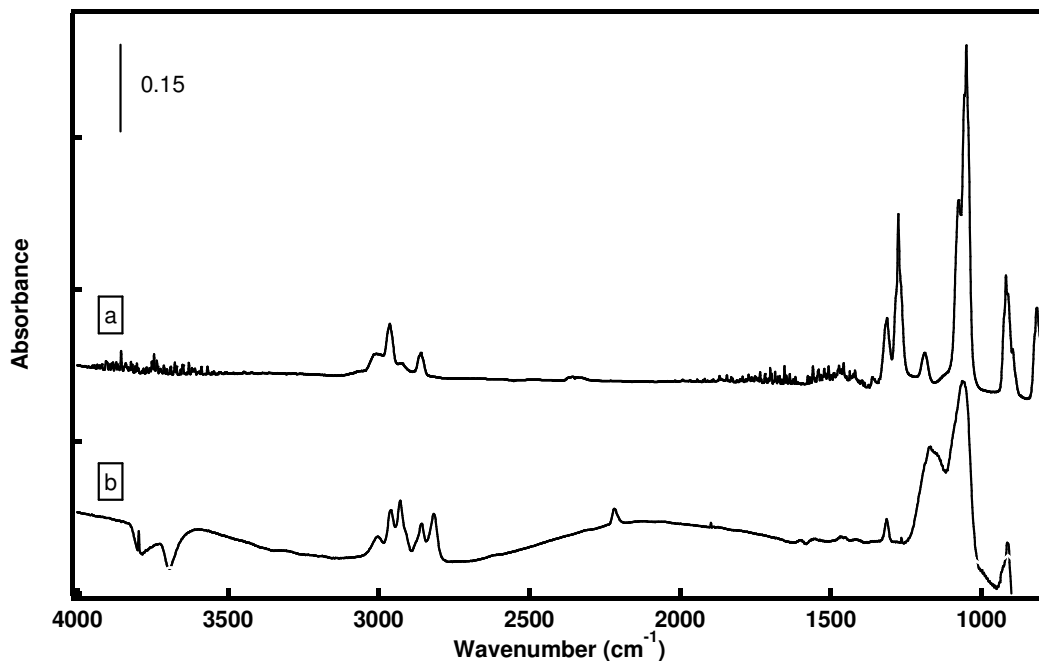


**Figure 4.17 Comparison of gas phase DMMP (a) to DMMP adsorption on 1.2 nm hafnium dioxide nanoparticles (b) at room temperature.**

To determine if particle size has any effect on reactivity, a spectrum of DMMP on 1.2 nm nanoparticles is compared to a spectrum of DMMP on 2.3 nm nanoparticles with the same exposure to DMMP. In the spectra shown in Figure 4.18, the (P=O) stretch at  $1210\text{ cm}^{-1}$  represents the physisorbed DMMP species and the asymmetric (O-P-O) stretch at  $1175\text{ cm}^{-1}$  results from the chemisorbed bridging species. Because the peaks are fairly broad, quantitative data is difficult to ascertain. These preliminary results indicate that the smaller particles are more reactive, signified by their higher proportion of chemisorbed DMMP to physisorbed DMMP.

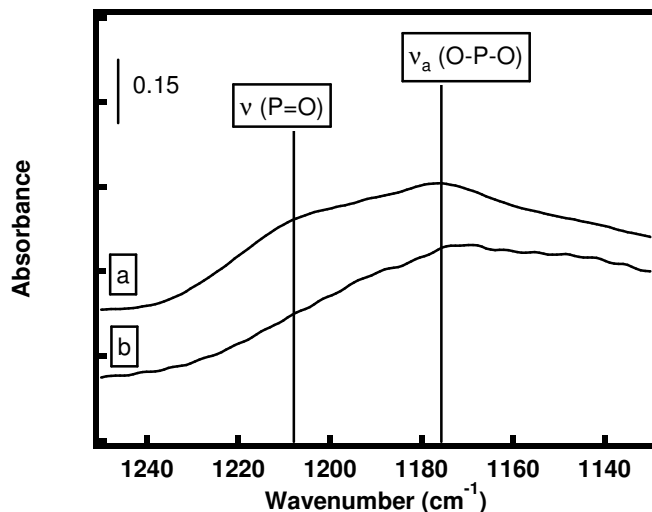


**Figure 4.18 Comparison of DMMP reactivity after 130 Langmuir of exposure on larger (a) and smaller (b) hafnium dioxide nanoparticles. Larger particles show similar uptake of DMMP, but have a higher percentage of physisorbed, unreacted DMMP while the 1.2 nm HfO<sub>2</sub> particles show a higher percentage of chemisorbed DMMP bound to the surface.**

#### 4.2.11 Hafnium Dioxide Nanoparticles Made in an Oxygen Backfill

Vacancy defect sites have been hypothesized to be the most reactive sites on metal oxide nanoparticles.<sup>70</sup> To test this theory, hafnium dioxide nanoparticles were synthesized in an oxygen backfill of 10 Torr and should have fewer defect sites than nanoparticles made in 10 Torr of nitrogen. Yates et al. has shown that annealing a TiO<sub>2</sub> surface in an oxygen flux followed by cooling will oxidize any vacancy sites and create a more perfect lattice.<sup>70</sup> Nanoparticles were synthesized in 10 Torr of O<sub>2</sub> and then exposed to approximately 170 Langmuir of DMMP at room temperature. As shown in Section 3.3, particle synthesized in oxygen had a particle size of 3.2 nm. This particle size is slightly larger than HfO<sub>2</sub> nanoparticles synthesized in 10 Torr of nitrogen, which was 2.3 nm. The positive peaks in the difference spectrum show that DMMP has adsorbed onto the hafnium dioxide nanoparticles. The high energy region of the spectrum in Figure 4.19 shows that the oxygen synthesized nanoparticles have similar adsorption and

reactivity characteristics as their analogs synthesized in nitrogen. This indicates that DMMP is adsorbing and reacting to form a surface methoxy group and a bridging O-P-O species on these larger nanoparticles with a potentially lower number of oxygen vacancy sites. The lower frequency region shows similar reactivity (not shown).

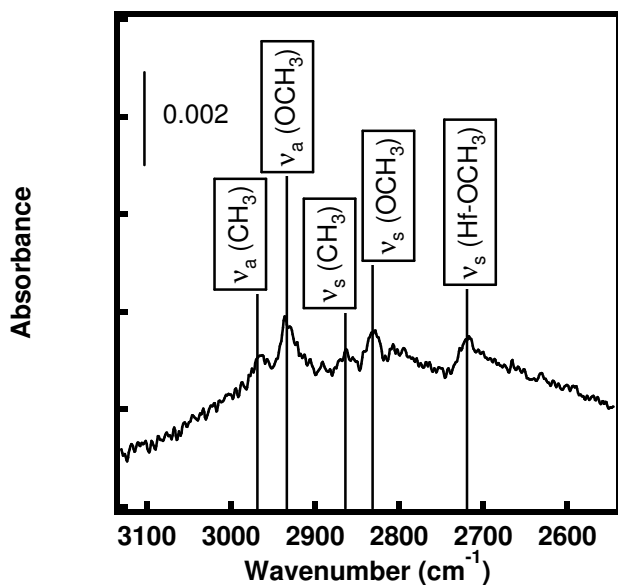


**Figure 4.19 High frequency region of DMMP adsorbed on oxygen synthesized 3.2 nm hafnium dioxide nanoparticles.**

Figure 4.20 displays the spectrum of 3.2 nm hafnium dioxide nanoparticles synthesized in oxygen exposed to 170 Langmuir of DMMP compared to 1.2 nm nanoparticle synthesized in nitrogen exposed to 130 Langmuir of DMMP. Even though the larger particles were exposed to much more DMMP, they exhibited much less uptake. This leads to the conclusion that oxygen vacancy sites are likely important components in the uptake and reactivity of DMMP on hafnium dioxide nanoparticles. Defect sites corresponding to varying oxidation states of hafnium may be important to reactivity.

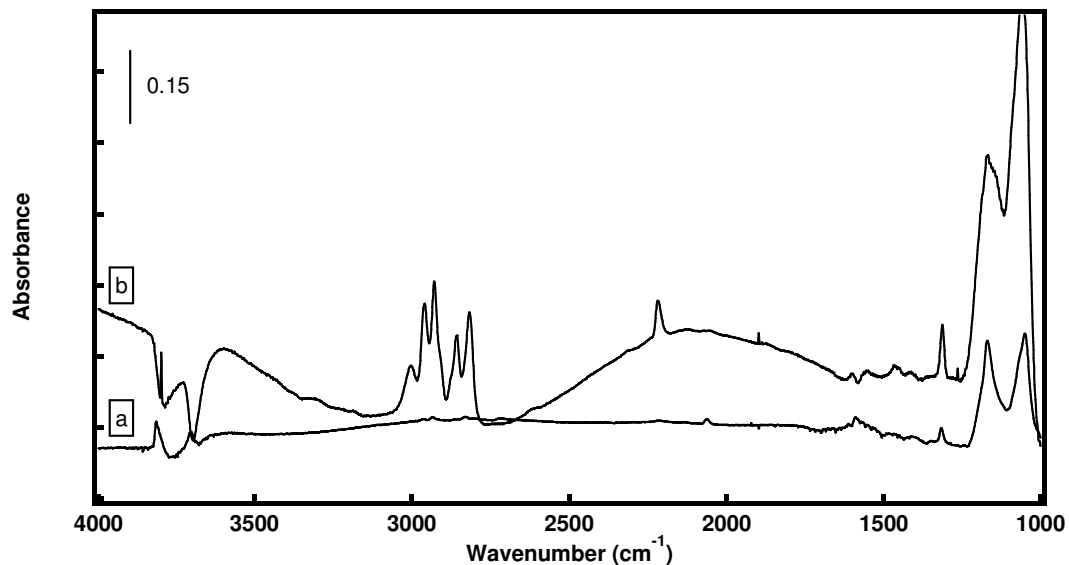


**Figure 4.20 Comparison of DMMP exposed to larger, oxygen synthesized nanoparticles (a) and smaller, nitrogen synthesized nanoparticles (b).**

#### **4.2.12 Hafnium Dioxide Nanoparticles Annealed to 500K and then Exposed to DMMP**

A mechanism has been proposed that implicates residual surface hydroxyl groups bound to surface hafnium ions as the initial site for adsorption.<sup>33</sup> As seen in Figure 4.5, surface hydroxyl groups are removed from the surface as DMMP adsorbs on HfO<sub>2</sub> nanoparticles, which may be the source of initial physisorption. To test this theory, nanoparticles were heated and cooled before exposure to DMMP to remove residual hydroxyl groups. Hafnium dioxide nanoparticles were created in 1 Torr of nitrogen and transferred to the analysis chamber without exposing them to the atmosphere. Once they were transferred to the sample mount, the particles were heated to 500K for six hours and cooled to room temperature before exposing them to DMMP. This has been shown to remove residual hydroxyl groups from a metal oxide surface.<sup>70</sup> Heating the nanoparticles to this high temperature likely does not change the size and shape; however, AFM analysis could not be performed, so this remains a possibility. After the surface was

heated and cooled to room temperature, the difference spectrum had two negative peaks, indicating that many of the hydroxyl groups were removed, as well as some of the residual surface carbonate contaminants (not shown). The pre-annealed surface was used as the background for the difference spectrum and then the surface was exposed to approximately 170 Langmuir of DMMP. The cooled nanoparticles show a high frequency C-H stretching region from 2800 to 3010  $\text{cm}^{-1}$  with five peaks, indicating that a surface-bound methoxy is a product of this reaction (not shown). While there is evidence for decomposition, comparison of a spectrum of DMMP adsorbed to annealed and cooled nanoparticles to DMMP adsorbed to as-prepared hafnium dioxide nanoparticles (Figure 4.21), it is clear that the uptake is reduced. The peak intensities were much lower, though the annealed and cooled nanoparticles were exposed to 40 additional Langmuir of DMMP.

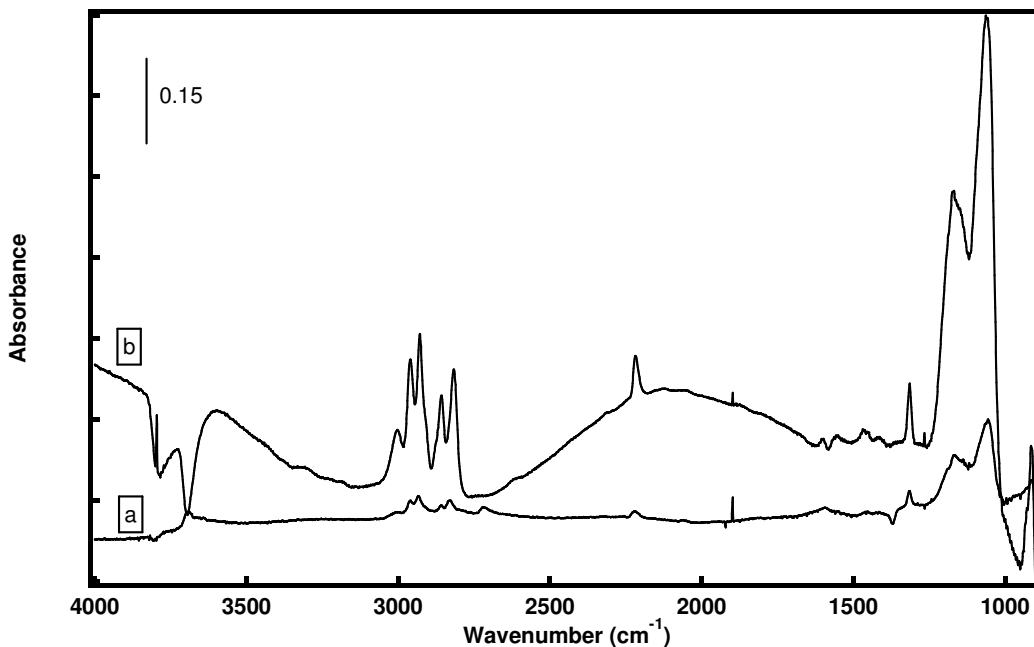


**Figure 4.21 Comparison of DMMP adsorption on annealed and cooled nanoparticles (a) and unannealed nanoparticles (b). The annealed and cooled nanoparticles were exposed to 170 Langmuir of DMMP, while the as-prepared nanoparticles were exposed to 130 Langmuir of DMMP.**

DMMP adsorbs and decomposes on the annealed and nanoparticles with both physisorbed and chemisorbed species as seen in Figure 4.12. Furthermore, Figure 4.22 demonstrates that the intensities of the modes associated with the O-H stretch increase along with the DMMP peaks, implying a correlation between O-H and DMMP uptake. In order for the reaction to occur, there must be water adsorbed on the surface, which most likely results from water entrained in the reservoir of the hydrophilic DMMP, though the low level of water could not be detected by the residual gas analyzer. Once the surface hydroxyls are present on the surface, as indicated by the positive peaks in the O-H stretching region, at  $3650\text{ cm}^{-1}$ , DMMP uptake on the surface occurs and the reaction proceeds as seen on as-prepared nanoparticles. This supports the hypothesis that surface hydroxyl groups are necessary for initial DMMP adsorption.

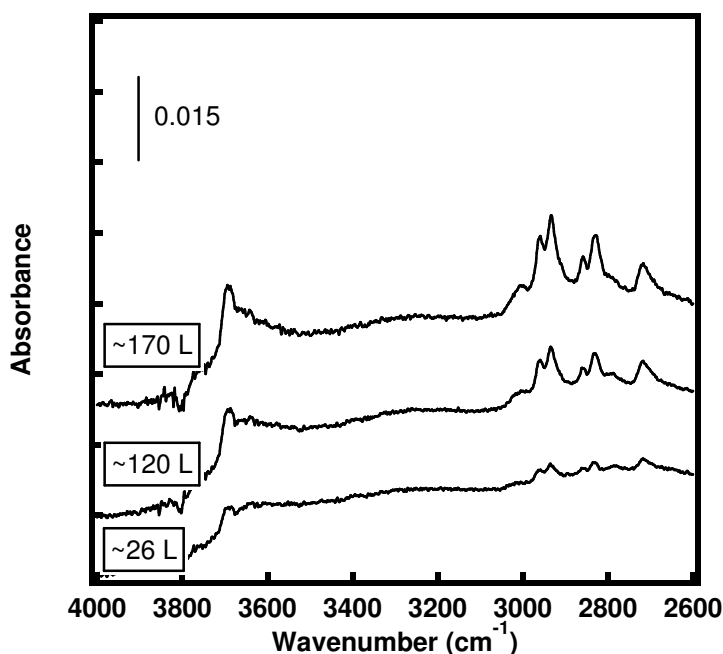


**Figure 4.22 C-H stretching region of DMMP adsorption on 2.3 nm HfO<sub>2</sub> nanoparticles at difference exposures. Surface reactivity of DMMP occurs as surface hydroxyl groups ( $3650\text{ cm}^{-1}$ ) increase in intensity.**

### 4.3 Conclusions

The purpose of this study was to determine the fundamental interactions of DMMP with hafnium dioxide nanoparticles and establish how residual functionalities on the surface influence uptake and reactivity. Hafnium dioxide nanoparticles were synthesized by the inert gas phase condensation method, enabling the control of the particle size via background pressure. AFM analysis determined that particles synthesized under 1 and 10 Torr of nitrogen had mean particle sizes of  $1.2 \pm 0.8$  nm and  $2.3 \pm 0.8$  nm, respectively. Particles synthesized under 1 Torr of oxygen were even larger with a mean particle size of  $3.2 \pm 1.5$  nm. This large standard deviation could be due to a bimodal distribution of particle sizes, though current experimental evidence has not been able to confirm this. The nanoparticles grow very interesting thin film morphologies. If nanoparticles are synthesized in 1 Torr of nitrogen, the nanoparticles aggregate in fluffy, tree-like structures on the surface, whereas if they are synthesized in 10 Torr of nitrogen, result in a much more dense, web-like structures result as determined by SEM.

Dimethyl methylphosphonate adsorbs on the hafnium dioxide nanoparticles and decomposes via a surface reaction. For 2.3 nm particles, there was a significant portion of physisorbed DMMP, which had adsorbed to the surface but not reacted, as well as chemisorbed DMMP, which had undergone a surface reaction resulting in the breaking of a P-OMe bond to form a surface bound methoxy group and a bridging oxygen-phosphorus-oxygen species. Results indicate that a greater fraction of the adsorbed DMMP had reaction on the smaller, 1.2 nm particles.

In the IR difference spectrum recorded as DMMP was exposed to the surface, the O-H stretching peak generally decreases as the adsorbed DMMP IR peaks increase, indicating that surface bound hydroxyl groups are affected by the uptake of DMMP, shown in Figure 4.5 and 4.17. Annealed hafnium dioxide surfaces, with a lower concentration of surface hydroxyl groups, showed reduced uptake of DMMP; however, cleavage of the O-CH<sub>3</sub> bond still occurred in a small amount (Figure 4.21). Studies of hafnium dioxide nanoparticles synthesized in oxygen, with more oxygen and less anion vacancy sites, indicated reduced uptake of DMMP, though the reactivity of the particles was not suppressed. The reduced uptake may indicate that anion vacancy sites in the HfO<sub>2</sub> lattice are necessary for initial binding, though once a molecule is adsorbed on to the nanoparticle, decomposition to a surface methoxy and a bridging oxygen-phosphorus-oxygen species occurs similarly to reactivity on the as-prepared nanoparticles.

Perhaps the most interesting results were shown in Section 4.2.12. HfO<sub>2</sub> nanoparticles synthesized in 1 Torr of nitrogen were annealed to 500K and then cooled to room temperature before being exposed to 170 Langmuir of DMMP. Even though these nanoparticles were exposed to 40 Langmuir addition DMMP before saturation appeared to occur, their uptake was minimal compared to nanoparticles that had not been annealed. It was also observed that with continued dosing of DMMP, a peak at 3650 cm<sup>-1</sup> increased in intensity, corresponding to an increase in surface hydroxyl groups. It appears that a surface O-H functionality is necessary to the uptake of DMMP, though the concentration of these groups or their specific role in binding has yet to be determined.

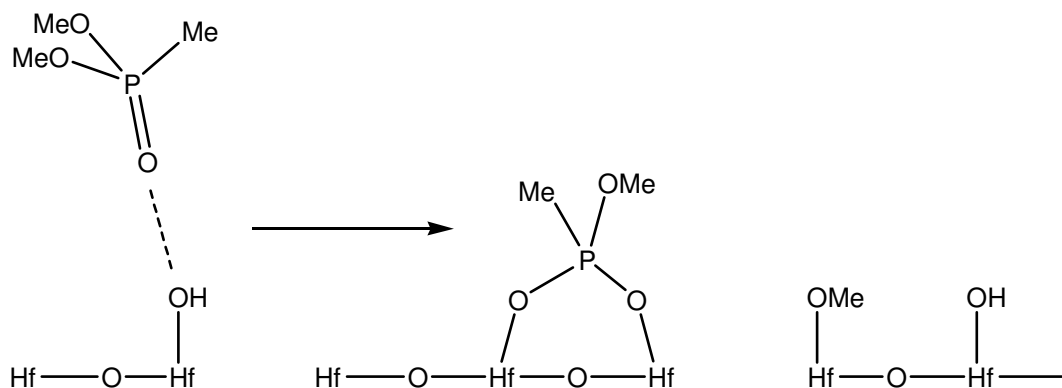


**Figure 4.23 DMMP adsorbs and reacts on HfO<sub>2</sub> nanoparticles at room temperature. Similar reactivity is seen on nanoparticles made in an oxygen atmosphere as well as nanoparticles annealed and cooled before DMMP exposure, though the uptake on these particles is greatly diminished.**

The following mechanism has been suggested by Mitchell,<sup>33</sup> an electrophilic substitution reaction that involves residual surface hydroxyl groups. Studies presented in this thesis support surface hydroxyl groups as a necessary component for reactivity. When HfO<sub>2</sub> nanoparticles were annealed and cooled before exposure, uptake and reaction only occurred as hydroxyl groups on the surface increased in intensity. The increase in concentration may come from two possible sources: residual water in the reservoir of DMMP used for dosing, and water bound to the walls and surfaces of the ultra-high vacuum analysis chamber. The Mitchell mechanism<sup>33</sup> suggests two final products, a bridging O-P-O species and a surface-bound methoxy group, though the decomposition does not occur at room temperature. RAIRS studies in this thesis support the formation of these two surface products, though reactivity was extensively observed at room temperature.

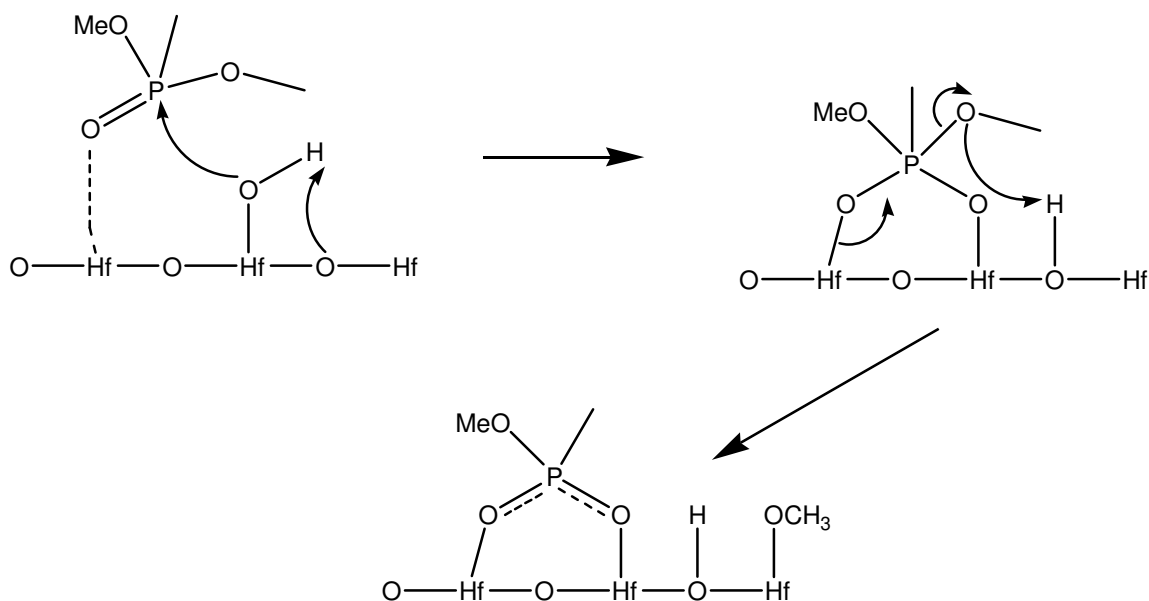


**Figure 4.24 Possible mechanism of DMMP reacting on HfO<sub>2</sub>.**<sup>33</sup>

#### 4.4 Future Work

The goal of this body of work includes a detailed understanding of the reaction mechanism between the chemical warfare agent stimulant DMMP and a variety of metal oxide nanoparticles and to understand how properties of the surface, such as hydroxyl concentrations and defect sites, affect this reactivity. Future work includes a more detailed particle size study, which has been suggested as a source of increased reactivity in this work already. Temperature dependent studies must be performed to determine how temperature affects uptake, and if reaction will occur at low temperature. Exposing a cold surface to DMMP would result in spectra of physisorbed DMMP. As the temperature is raised, DMMP will decompose on the surface. This type of study could give additional insight into the decomposition mechanism. A detailed XPS study could also provide insight into the presence of oxygen defects by analysis of oxidation states of hafnium for particles synthesized in different background gases. These should be exposed to varying concentrations of DMMP to determine if oxygen defect

concentrations influences uptake or reactivity of DMMP. The role of surface hydroxyls in the reaction mechanism could be studied by annealing the surface to remove the surface bound water and dosing with D<sub>2</sub>O. Labeling the oxygens of DMMP with O<sup>18</sup> could give insight as to where these elements end up in the final surface bound products.

## References

- (1) Yang, Y.-C. B., James A.; Ward, J. Richard *Chemical Reviews* **1992**, 92, 1729-1743.
- (2) Anslow, W. P.; D.A.Karnofsky; Jager, B. W.; Smith, H. W. *Journal of Pharmacological and Experimental Therapy* **1948**, 93, 1-9.
- (3) Papirmeister, B.; Feister, A. J.; Robinson, S. I.; Ford, R. D. *Medical Defense Against Mustard Gas: Toxic Mechanisms and Pharmacological Implications*; CRC Press, Inc: Boca Raton, FL, 1991.
- (4) Compton, J. A. F. *Military Chemical and Biological Agents: Chemical and Toxicological Properties*; The Telford Press: Caldwell, NJ, 1987.
- (5) Demilitarization, U. A. O. o. t. P. M. f. C.; Army, U., Ed.: Maryland: Aberdeen Proving Ground, 1994.
- (6) Yang, Y.-C. *Chemistry and Industry* **1995**, 334-338.
- (7) McWilliams, J. L.; Steel, R. J. *The Battle of Ypres, 1915*; Vanwell Publishing Limited: Deyell Co., Canada, 1985.
- (8) Yang, Y.-C.; Szafraniec, L. L.; Beaudry, W. T.; Ward, J. R. *Journal of Organic Chemistry* **1988**, 53, 3293-3297.
- (9) Yang, Y.-C.; Szafraniec, L. L.; Beaudry, W. T.; Ward, J. R. *Journal of Organic Chemistry* **1990**, 55, 3664-3666.
- (10) Richardson, D. E.; Yao, H.; Frank, K. M.; Bennett, D. A. *Journal of the American Chemical Society* **2000**, 122, 1729-1739.
- (11) Wagner, G. W. Y., Yu-Chu *Ind. Eng. Chem. Res.* **2002**, 41, 1925-1928.
- (12) Wagner, G. W. P., Lawrence R. Yang, Yu-Chu; Bunton, Clifford, A. *Langmuir* **2001**, 17, 4809-4811.
- (13) McCoy, M. *Chemical and Engineering News* **1999**, 77, 18-19.
- (14) Epstein, J.; Demek, M. M.; Rosenblatt, D. H. *Journal of Organic Chemistry* **1956**, 21, 796-797.
- (15) Yang, Y.-C. S., Linda L.; Beaudry, William T. *Journal of Organic Chemistry* **1993**, 58, 6964-6965.
- (16) DeFrank, J. J. In *Applications of Enzyme Biotechnology*; Kelly, J. W., Baldwin, T. O., Eds.; Plenum Press: New York, 1991, pp 165-180.
- (17) Benschop, H. P.; Jong, L. P. A. D. *Accounts of Chemical Research* **1988**, 21, 368-374.
- (18) Yang, Y.-C. *Accounts of Chemical Research* **1999**, 32, 109-115.
- (19) Yang, Y.-C. B., Frederic J.; Szafraniec, Linda L.; Beaudry, William T.; Bunton, Clifford A.; Kumar, Anurag *Journal of the Chemical Society, Perkins Transitions 2* **1997**, 607-613.
- (20) Bell, A. T. *Science* **2003**, 299, 1688-1691.
- (21) "Nanoscale Science, Engineering and Technology Research Directions," Office of Basic Energy Sciences.
- (22) Jefferson, D. A.; Tilley, E. E. M. In *Particulate Matter*; Maynard, R. L., Howard, C. V., Eds.; BIOS Scientific Publishers: Oxford, 1999, pp 63-84.
- (23) Klabunde, K. J. *Free Atoms, Clusters, and Nanoscale Particles*; Academic Press: San Diego, CA, 1994.

- (24) Klabunde, K. J.; Stark, J.; Koper, O.; Mohs, C.; Park, D. G.; Decker, S.; Jiang, Y.; Lagadic, I.; Zhang, D. *Journal of Physical Chemistry* **1996**, *100*, 12142-12153.
- (25) Atteya, M.; Klabunde, K. J. *Chemistry of Materials* **1991**, *3*, 182-187.
- (26) Lucas, E.; Decker, S.; Khaleel, A.; Seitz, A.; Fultz, S.; Ponce, A.; Li, W.; Carnes, C.; Klabunde, K. J. *Chemistry- A European Journal* **2001**, *7*, 2505-2510.
- (27) Wagner, G.; Procell, L.; Koper, O.; Klabunde, K. In *Defense Applications of Nanomaterials*; Miziolek, A., Karna, S., Mauro, J. M., Vaia, R. A., Eds.; Oxford University Press: Washington DC, 2005, pp 139-151.
- (28) Michalkova, A. I., M.; Gorb, L.; Leszczynski, J. *Journal of Physical Chemistry B* **2004**, *108*, 5294-5303.
- (29) Zhanpeisov, N. U.; Zhidomirov, G. M.; Yudanov, I. V.; Klabunde, K. J. *Journal of Physical Chemistry* **1994**, *98*, 10032-10035.
- (30) Lin, S.-T.; Klabunde, K. J. *Langmuir* **1985**, *1*, 600-605.
- (31) Rajagopalan, S.; Koper, O.; Decker, S.; Klabunde, K. J. *Chemistry - A European Journal* **2002**, *8*, 2602-2607.
- (32) Li, Y.-X.; Schlup, J. R.; Klabunde, K. J. *Langmuir* **1991**, *7*, 1394-1399.
- (33) Mitchell, M. B.; Sheinker, V. N.; Mintz, E. A. *Journal of Physical Chemistry B* **1997**, *101*, 11192-11203.
- (34) Li, Y.-X.; Klabunde, K. J. *Langmuir* **1991**, *7*, 1388-1393.
- (35) Templeton, M. K.; Weinberg, W. H. *Journal of the American Chemical Society* **1985**, *107*, 97-108.
- (36) Templeton, M. K.; Weinberg, W. H. *Journal of the American Chemical Society* **1985**, *107*, 774-779.
- (37) Kozlov, D. V. V., A.V.; Smirniotis, P.G.; Savinov, E.N. *Applied Catalysis B: Environmental* **2003**, *42*, 77-87.
- (38) Panayotov, D. A.; Paul, D. K.; Jr., J. T. Y. *Journal of Physical Chemistry B* **2003**, *107*, 10571-10575.
- (39) Kim, C. S.; Lad, R. J.; Tripp, C. P. *Sensors and Actuators B* **2001**, *76*, 442-448.
- (40) Trubitsyn, D. A.; Vorontsov, A. V. *Journal of Physical Chemistry B* **2005**, *109*, 21884-21892.
- (41) Rusu, C. N.; John T. Yates, J. *Journal of Physical Chemistry B* **2000**, *104*, 12292-12298.
- (42) Kuiper, A. E. T.; Bokhoven, J. J. G. M. V.; Medema, J. *Journal of Catalysis* **1976**, *43*, 154-167.
- (43) Mars, P.; Krevelen, D. W. V. *Chemical Engineering Science* **1954**, *3*, 41.
- (44) Fernandez, A.; Reddy, E. P.; Rojas, T. C.; Sanchez-Lopez, J. C. *Vacuum* **1999**, *52*, 83-88.
- (45) Nakata, Y.; Muramoto, J.; Okada, T.; Maeda, M. *Journal of Applied Physics* **2002**, *91*, 1640-1643.
- (46) Nakata, Y.; Kaibara, H.; Okada, T.; Maeda, M. *Journal of Applied Physics* **1996**, *80*, 2458.
- (47) Wilk, G. D.; Wallace, R. M.; Anthony, J. M. *Journal of Applied Physics* **2001**, *89*, 5243-5275.
- (48) Sayan, S.; Garfunkel, E.; Suzer, S. *Applied Physics Letters* **2002**, *80*, 2135.

- (49) Bastos, K. P.; Morais, J.; Miotti, L.; Pezzi, R. P.; Soares, G. V.; Baumvol, I. J. R.; Hegde, R. I.; Tseng, H. H.; Tobin, P. J. *Applied Physics Letters* **2002**, *81*, 1669-1671.
- (50) Salem, I. *Catalysis Reviews* **2003**, *45*, 205-296.
- (51) Onishi, Y.; Iizuka, Y.; Hamamura, T. *Bulletin of the Chemical Society of Japan* **1980**, *53*, 263-264.
- (52) Kulkarni, D.; Wachs, I. E. *Applied Catalysis A: General* **2002**, *237*, 121-137.
- (53) Hussein, G. A. M.; Sheppard, N.; Zaki, M. I.; Fahim, R. B. *Journal of the Chemical Society, Faraday Transactions* **1991**, *87*, 2655-2659.
- (54) Esphlandiu, M. J.; Patrio, E. M.; Macagno, V. A. *Electrochemical Acta* **1997**, *42*, 1315.
- (55) Capone, S.; Leo, G.; Rella, R.; Siciliano, P.; Vasanelli, L.; Alvisi, M.; Mirengi, L.; Rizzo, A. *Journal of Vacuum Science and Technology A* **1998**, *16*, 3564-3568.
- (56) DiGiulio, M.; Micocci, G.; Serra, A.; Tepore, A.; Rella, R.; Siciliano, P. *Journal of Vacuum Science and Technology A* **1996**, *14*, 2215.
- (57) Swihart, M. T. *Current Opinion in Colloid and Interface Science* **2003**, *8*, 127-133.
- (58) Grieve, K.; Mulvaney, P.; Greiser, F. *Current Opinion in Colloid and Interface Science* **2000**, *5*, 168-172.
- (59) Trindade, T.; O'Brien, P.; Pickett, N. L. *Chemical Materials* **2001**, *13*, 3843-3858.
- (60) Wegner, K.; Walker, B.; Tsantilis, S.; Pratsinis, S. E. *Chemical and Engineering Science* **2002**, *57*, 1753-1762.
- (61) Binnig, G.; Quate, C. F.; Gerber, C. *Physical Review Letters* **1986**, *56*, 930.
- (62) Binnig, G.; Gerber, C.; Stoll, E.; Albrecht, T. R.; Quate, C. F. *Europhysics Letters* **1987**, *3*, 1281.
- (63) Birdi, K. S. *Scanning Probe Microscopies*; CRC Press: Boca Raton, Florida, 2003.
- (64) Goldstein, J. I.; Newbury, D. E.; Echlin, P.; Joy, D. C.; Lyman, C. E.; Lifshin, E.; Sawyer, L.; Michael, J. *Scanning Electron Microscopy and X-ray Microanalysis*; 3rd ed.; Kluwer Academic / Plenum Publishers: New York, NY, 2003.
- (65) Ellis, A.; Feher, M.; Wright, T. *Electronic and Photoelectron Spectroscopy*; Cambridge University Press: Cambridge, 2005.
- (66) Greenler, R. G. *Journal of Chemical Physics* **1966**, *44*, 310-315.
- (67) Greenler, R. G. *Journal of Chemical Physics* **1969**, *50*, 1963-1968.
- (68) Tanabe, K. **1970**.
- (69) Koper, O.; Lagadic, I.; Klabunde, K. J. *Chemistry of Materials* **1997**, *9*, 2468-2480.
- (70) Thompson, T. L. D., Oliver; Yates, John T. *Journal of Physical Chemistry B* **2003**, *107*, 11700-11704.
- (71) Lam, H. M.; Hong, M. H.; Yuan, S.; Chong, T. C. *Applied Physics A* **2004**, *79*, 2099-2102.

- (72) Ekerdt, J. G. K., K.J.; Shapley, J.R.; White, J.M.; Yates, J.T. *Journal of Physical Chemistry* **1988**, *92*, 6182-6188.
- (73) Tesfai, T. M.; Sheinker, V. N.; Mitchell, M. B. *Journal of Physical Chemistry B* **1998**, *102*, 7299-7302.
- (74) Li, Y.-X. K., Kenneth J. *Langmuir* **1991**, *7*, 1388-1393.
- (75) Guo, X. Y., J.; Yayas, J.T. *Journal of Physical Chemistry* **1990**, *94*, 6839-6842.
- (76) Mitchell, M. B.; Sheinker, V. N.; Tesfamichael, A. B.; Gatimu, E. N.; Nunley, M. *Journal of Physical Chemistry B* **2003**, *107*, 580-586.
- (77) Sheinker, V. N.; Mitchell, M. B. *Chemistry of Materials* **2002**, *14*, 1257-1268.
- (78) Moss, J. A.; Szczepankiewicz, S. H.; Park, E.; Hoffmann, M. R. *Journal of Physical Chemistry B* **2005**, *109*, 19779-19785.
- (79) Aurian-Blajeni, B.; Boucher, M. M. *Langmuir* **1989**, *5*, 170-174.
- (80) Zhou, J.; Ma, S.; Kang, Y. C.; Chen, D. A. *Journal of Physical Chemistry B* **2004**, *108*, 11633-11644.
- (81) Kanan, S. M.; Tripp, C. P. *Langmuir* **2001**, *17*, 2213-2218.
- (82) Moulder, J. F. *Handbook of X-Ray Photoelectron Spectroscopy*; FIX ME: FIX ME, 1995.
- (83) Mynbaeva, M.G.; Mynbaev, K.D.; Ivantsov, V.A.; Lavrent'ev, A.A.; Grayson, B.A.; Wolan, J.T. *Semiconductor Sci. and Tech.* **2003**, *18*, 602-606.
- (84) Moravie, R. M.; Froment, F.; Corset, J. *Spectrochimica Acta* **1989**, *45A*, 1015-1024.
- (85) Henderson, M. A.; White, J. M. *J. Am. Chem. Soc.* **1988**, *110*, 6939-6947.
- (86) George, L.; Sankaran, K.; Viswanathan, K. S.; Mathews, C. K. *Applied Spectroscopy* **1994**, *48*, 7-12.
- (87) Reva, I.; Simão, A.; Fausto, R. *Chem. Phys. Lett.* **2005**, *406*, 126-136.
- (88) Marsault-Herail, F. *Journal de Chimie Physique et de Physico-Chimie Biologique* **1971**, *68*, 274-286.